ASCE International Journal of Geomechanics. Submitted Dec 2020; Published Jan 2022.
https://doi.org/10.1061/(ASCE)GM.1943-5622.0002308

Stochastic assessment of landslide influence zone by material point method and generalized geotechnical random field theory

Guotao Ma[1], Mohammad Rezania[2], Mohaddeseh Mousavi Nezhad[3]

Abstract

In landslide analysis, reliable prediction of landslide's influence zone is significantly difficult due to inherent heterogeneity of soils and their spatially varying geological properties. In this paper, a probabilistic framework is proposed to evaluate the landslide hazard zoning through prediction of their influence zone considering the effects of heterogeneous soil properties. Material point method is used to simulate the large deformations during landslide failure. The spatial variation in the shear strength parameters of soils at undrained conditions is modeled by random fields, which are discretized by Cholesky matrix decomposition method to incorporate the effects of the soil spatial heterogeneity on the post-failure deformations. Furthermore, a practical landslide hazard zoning is conducted to quantitively evaluate the level of disaster for facilities or structures located in the vicinity of the slope by using the exceedance probability of influence distance and runout distance. Five categories based on different thresholds of exceedance probability are used to visualize the area potentially affected by the landslide. To demonstrate the capability of the stochastic

[1]Research Assistant, School of Engineering, University of Warwick, Coventry, UK.
Email: g.ma.1@warwick.ac.uk. ORCID: https://orcid.org/0000-0001-9783-413X
[2]Reader, School of Engineering, University of Warwick, Coventry, UK. (Corresponding Author)
Email: m.rezania@warwick.ac.uk. ORCID: https://orcid.org/0000-0003-3851-2442
[3]Reader, School of Engineering, University of Warwick, Coventry, UK.
Email: m.mousavi-nezhad@warwick.ac.uk. ORCID: https://orcid.org/0000-0002-0625-439X

assessment framework, a benchmark example of heterogeneous clayey slope is simulated, and the associated hazard zone is predicted and discussed; it presents a practical procedure for improving the landslide influence zone prediction and provides new insights for hazard zoning.

Keywords: Landslide, Influence zone, random field theory, material point method, hazard zoning

Introduction

Landslides are one of the most common natural geological hazards in the world (Huang and Fan 2013; Hungr et al. 2014). Thousands of slopes fail every year with detrimental consequences and significant damages to human life and properties (Ma et al. 2018; He et al. 2019). In many occasions, due to extensive runout of the landslides, substantial destruction can be observed on nearby structures (Yin et al. 2009, 2016). Landslide runout distance is one of the crucial factors that influences the level of disaster and there are many examples that confirm its devastating impacts during/after landslides. For instance, the 1966 Aberfan flowslide in the United Kingdom killed 144 people because of its extensive runout distance of about 640 m (Bishop et al. 1969). The 1972 Poshan road landslide in Hong Kong killed 73 people and destroyed 33 residential buildings by the sliding mass with a runout distance of approximately 1,100 m (Brand et al. 1984). The La Conchita landslide in the United States destroyed 9 homes in 1995 and killed 10 people in 2005 with its reactivated long runout sliding mass (Jibson 2006). The 2014 Oso landslide with the runout distance of about 1,000 m killed 43 people and destroyed 49 homes (Iverson et al. 2015). These examples show that the level of casualties and destruction of structures or facilities are directly influenced by the post-failure behavior of landslides. Understanding post-failure behavior of landslides is significantly important as it allows for the prediction of possible catastrophic consequences and timely planning of the disaster mitigation measures. For disaster mitigation and

resource planning of critical infrastructures located in the vicinity of slopes, it is crucial to rank the potential landslides and quantify the related hazard levels. This ranking allows to prioritize mitigation actions for the landslides with high failure probability and catastrophic consequences. Thus, this paper is dedicated to consequence assessment of landslides, post-failure, and to invesitage how serious damages of landslides after failure .

In engineering geology, variability of natural geomaterials (e.g. sand, silt, clay) is widely admitted. It has been proved that the spatial variability of the soil hydromechanical attributes notably influences the likelihood of the landslides (Hicks and Samy 2002), as well as their failure modes and mechanisms (Zhu and Zhang 2013), and subsequently affects on the post-failure behavior and runout motions. Experimental investigations together with geostatistical analyses proved that hydromechanical properties of the soils can be defined by multivariate random function characterized by spatial scale of fluctuation (named also correlations lengths), such that values of these attributes at points separated by distances much larger than the scale of the fluctuations are uncorrelated (Vanmarcke 1977, 2010; Mousavi Nezhad 2010). For instance, the spatial variability of shear strength of the soils could entail scales of fluctuation ranging from less than 1 m to tens of meters along different directions (Lacasse and Nadim 1997). Random field (RF) modeling is widely used in analyzing uncertainties of geotechnical properties (Mousavi Nezhad et al. 2013, 2018) and widely integrated with limit equilibrium method (LEM) (e.g. Mafi et al. 2020) and finite element method (FEM) (e.g., Griffiths and Fenton 2004; Jiang et al. 2014; Masoudian et al. 2019). In recent years, many probabilistic analyses have been conducted to investigate the effects of soil heterogeneity on the landslide modeling. Zhang et al. (2018) summarized the recent developments in probabilistic assessment of the slope failure, in which landslide instability or corresponding probability of failure (P_f) are mainly evaluated by the two abovementioned methods (i.e., LEM

and FEM). Among these studies, it can be noticed that modeling the consequences of the landslide hazards are still an open question. The main obstacle is how to include the spatial variability of the soil properties in the modeling algorithm in a computationally efficient and reliable manner. Part of the modeling challenges is related to the numerical instability of the classical Lagrangian modeling algorithms (e.g., Galerkin FEM algorithms) due to mesh distortion or twisting that occurs when simulating large deformation problems. The other issue is describing random parameters with appropriate geostatistical functions and parameters and implementing them into the large deformation modeling algorithms in the statistically and numerically consistent manner. As a result, a limited number of modeling frameworks have been developed so far for simulation of the post-failure processes in heterogeneous landslides or slope failures and their resulting consequences.

Recent progress in developing mesh-free particle methods, such as smoothed particle hydrodynamics (SPH) method (Nonoyama et al. 2015) and material point method (MPM) (Yerro et al. 2015; Soga et al. 2016), made it possible to tackle the numerical instability issues associated with the mesh distortion problems. MPM uses a combination of Lagrangian particles and Eulerian background computational mesh to avoid excessive mesh distortions issues that emerge in solving the partial differential equations of problems involving large deformations. The success of the MPM in reliably modeling the large deformation phenomena attracted researchers to adopt this method for modeling of landslides, slope failures, embankment collapse, and other large strain geological and geotechnical problems (e.g., Andersen and Andersen 2010; Wang et al. 2016; Llano-Serna et al. 2016; Li et al. 2016). However, in the previous MPM studies, the materials have been mainly assumed to be simply homogeneous and isotropic, and the geomaterials' responses have been modeled deterministically using constant values of soil parameters. Recently, Wang

(2017) investigated two main slope failure mechanisms of a landslide by MPM and combined the MPM with RF theory to quantify the retrogressive distance (influence distance) from the slope crest. Liu et al. (2019) utilized the LEM and MPM combined with Monte Carlo (MC) simulations to quantify the failure probability of landslides and predict the slope failure modes. Liu et al. (2021) conducted postfailure analysis of isotropic deposited slopes by probabilistic MPM analysis.

In this study, an integrated computational framework based on the stochastic material point method is developed and implemented to simulate landslides and quantify their hazard zones. The aim is to incorporate the effects of the statistically complex spatial variability of the soil characteristics on modeling the failure process using a generalized RF concept. The landslide runout distance and influence distance are probabilistically estimated, and a hazard zoning analysis is adopted to evaluate the impact of the landslides on nearby developments and delineate hazard levels.

Methodology

Landslide's influence zone assessment framework

In what follows, a computational stochastic assessment framework is developed using RF theory within the context of MPM (henceforth referred to as stochastic MPM) for landslide influence zone analysis during the post-failure stage. The overall structure of the framework contains a) an algorithm to generate RF samples of the spatially variable soil properties; b) a modeling algorithm based on MPM for landslide simulation; and c) an MC simulation algorithm for the quantitative evaluation of the landslide influence zone.

ASCE International Journal of Geomechanics. Submitted Dec 2020; Published Jan 2022.
https://doi.org/10.1061/(ASCE)GM.1943-5622.0002308

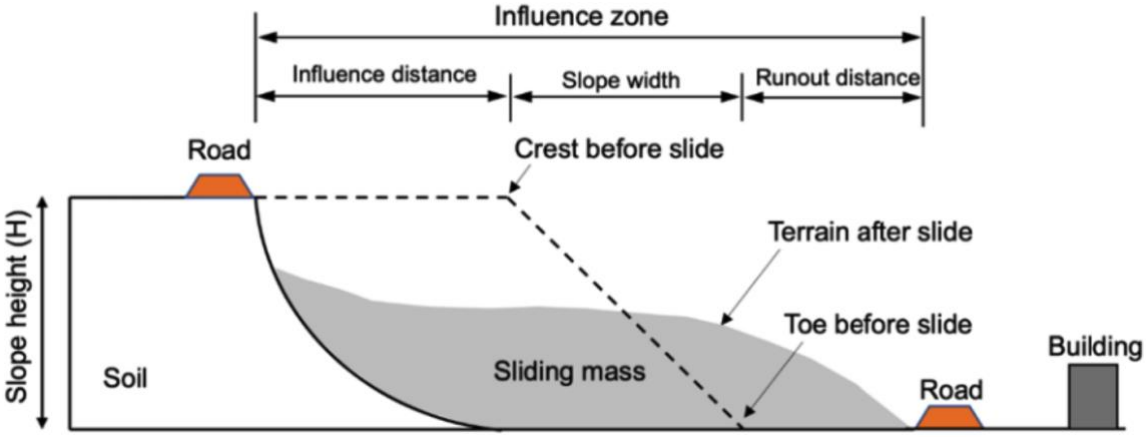

Fig. 1 Schematic view of the landslide influence distance (I) and runout distance (R)

The framework utilizes the risk aggradation methodology to rank the hazards. The predicted results from the probabilistic framework illustrate the soil behavior in the vicinity of the landslide initiation point which is quantified by failure parameters i.e., influence distances I and runout distances R as defined in Fig. 1. Multiple random samples are given to the framework to incorporate the spatial variability of the heterogeneous soil in the failure process modeling. The MPM applies to evaluate the influence distances from the slope crest and runout distances from slope toe for each sample, and the multiple outputs generated by the MC simulations are used to evaluate the statistical features of the failure parameters, and corresponding hazard zones for the structures or facilities (Fig. 2).

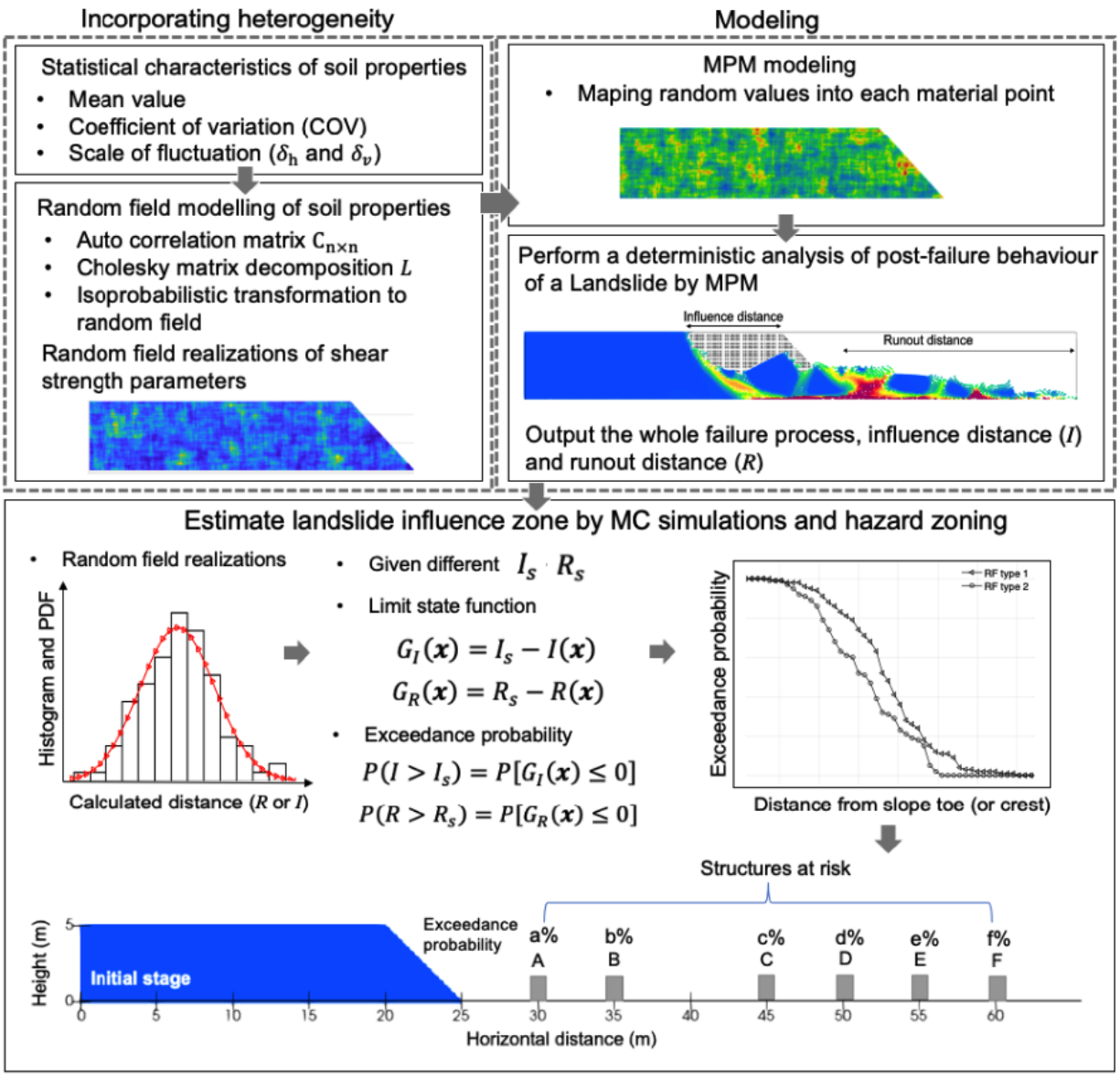

Fig. 2 Framework for evaluation of the influence zone of landslides

In general, if the landslide runout exceeds the distance between the structure at risk and the initial toe of the slope, the structure will certainly be affected by the landslide. The same is the case for a structure located at the crest of the slope that is susceptible to potential retrogressive failure. Therefore, it should be identifed whether the influence zone of a potential landslide will exceed a given threshold value in respect of influence distances I and runout distances R. Assuming there

are structures (e.g., railways, bridges, and residential buildings) located at distances R_s (or I_s) away from the toe (or crest) of the slope. A limit state function can be formulated

$$G_I(\boldsymbol{x}) = I_s - I(\boldsymbol{x}) \tag{1}$$

$$G_R(\boldsymbol{x}) = R_s - R(\boldsymbol{x}) \tag{2}$$

where $\boldsymbol{x}$ is a vector consisting of a generated RF sample considered in the model; $I(\boldsymbol{x})$ or $R(\boldsymbol{x})$ are the computed I or R associated with $\boldsymbol{x}$. Therefore, $G_I(\boldsymbol{x}) < 0$ means the influence distance of the landslide exceeds the threshold values and affects the structure (similarly for $G_R(\boldsymbol{x})$). Subsequently, the probability of the landslide impacting these structures can be expressed as $P(I > I_s)$ and $P(R > R_s)$, respectively.

$$P(I > I_s) = P[G_I(\boldsymbol{x}) \leq 0] = \int_{G_I(\boldsymbol{x}) \leq 0} f_x(\boldsymbol{x})\, \mathrm{d}\boldsymbol{x} \tag{3}$$

$$P(R > R_s) = P[G_R(\boldsymbol{x}) \leq 0] = \int_{G_R(\boldsymbol{x}) \leq 0} g_x(\boldsymbol{x})\, \mathrm{d}\boldsymbol{x} \tag{4}$$

where, $P(I > I_s)$ defines the exceedance probability of the cases in which the influence distance I exceeds I_s; $f_x(\boldsymbol{x})$ is the corresponding joint probability density function of $\boldsymbol{x}$, the integral is taken over the values of $\boldsymbol{x}$ that leads to $G_I(\boldsymbol{x}) \leq 0$; the $P(R > R_s)$ defines exceedance probability of the cases in which the runout distance R exceeds R_s; $g_x(\boldsymbol{x})$ is the corresponding joint probability density function of $\boldsymbol{x}$, the integral is taken over the values of $\boldsymbol{x}$ that leads to $G_R(\boldsymbol{x}) \leq 0$.

ASCE International Journal of Geomechanics. Submitted Dec 2020; Published Jan 2022.
https://doi.org/10.1061/(ASCE)GM.1943-5622.0002308

Landslide post-failure modeling

Governing equations

The numerical analysis of thermo-mechanical systems in the field of continuum mechanics initiates by establishing the idealized mathematical formulations using conservation laws and constitutive models. There are four conservation rules that should be satisfied over the problem domain and boundaries, namely (1) the conservation of mass, (2) the conservation of linear momentum, (3) the conservation of angular momentum, and (4) the conservation of energy. For the case of isothermal conditions, the conservation of mass and linear momentum leads to that of energy. Moreover, the conservation of angular momentum is proved by considering the symmetrical stress tensor. Therefore, only the conservation of mass and linear momentum, which is called momentum from now on, form the governing equations in the most cases. The derivations of these laws are out of the scope of this study, but can be found in detail in Reddy (2013).

Consider the problem domain Ω which is surrounded by boundary Γ. The boundary can be considered as the union of two displacement (Γ_u) and traction (Γ_t) boundaries. Without going through the derivation, the mathematical form of the conservation of mass and momentum laws can be written as follow over the problem domain and boundary

$$\frac{\partial \rho}{\partial t} + \rho \frac{\partial v_i}{\partial x_i} = 0 \tag{5}$$

$$\rho \frac{\partial v_i}{\partial t} = \frac{\partial \sigma_{ij}}{\partial x_j} + \rho b_i \tag{6}$$

Where, ρ is the mass density, v_i is the velocity, σ_{ij} is the *Cauchy* stress tensor, and b_i is the body force. Since Eq. (6) is in the strong form, finding a solution is almost impossible for complex practical problems. Thus, to achieve a weak form governing equation, the momentum equation

should be multiplied by a virtual displacement (δu_i) and it has to be integrated over the domain Ω. By applying Gauss's divergence theorem, the virtual work equation can be expressed as

$$\int_\Omega \delta u_{i,j} \rho \sigma_{ij}^s dV + \int_\Omega \delta u_i \rho \ddot{u}_i dV - \int_\Omega \delta u_i \rho b_i dV - \int_{\Gamma_t} \delta u_i \bar{t_i^S} \rho dA = 0 \tag{7}$$

where, u_i is displacement, σ_{ij}^s is the specific stress ($\sigma_{ij}^s = \sigma_{ij}/\rho$), $\bar{t_i^S}$ is the specific traction ($\bar{t_i^S} = \bar{t}_i/\rho$), and $\delta u_{i,j} = \partial(\delta u_i)/\partial x_j$.

Applied constitutive model

The accuracy and reliability of FEM analysis is significantly dependent on the appropriateness of the constitutive model used (e.g., Rezania et al. 2014, Rezania et al. 2018). The Drucker-Prager (D-P) constitutive model with strain softening feature is employed in this work to describe the geomaterial's behavior (Huang et al. 2015). The shear yield function F^s and tensile yield function F^t of the D-P yield criterion (as shown in Fig. 3a) are expressed as

$$F^s = \sqrt{J_2} + q_\varphi I_1 - k_c \tag{8}$$

$$F^t = \frac{I_1}{3} - \sigma^t \tag{9}$$

where, the q_φ and k_c are the parameters related to the internal friction angle φ and cohesion c of soil, J_2 is the second invariant of the deviatoric stress tensor, I_1 the first invariant of the stress tensor, and σ^t is the tensile strength. The q_φ and k_c are given by

$$q_\varphi = \frac{\tan\varphi}{\sqrt{9+12\tan^2\varphi}} \tag{10}$$

$$k_c = \frac{3c}{\sqrt{9+12\tan^2\varphi}} \tag{11}$$

ASCE International Journal of Geomechanics. Submitted Dec 2020; Published Jan 2022.
https://doi.org/10.1061/(ASCE)GM.1943-5622.0002308

The model uses a non-associated flow rule with shear potential function, G^s (for shear plastic flow) and tensile potential function, G^t(for tensile plastic flow) defined as

$$G^s = \sqrt{J_2} + q_\psi I_1 \tag{12}$$

$$G^t = \frac{I_1}{3} \tag{13}$$

where

$$q_\psi = \frac{\tan\psi}{\sqrt{9+12\tan^2\psi}} \tag{14}$$

where, the ψ is the dilation angle, the q_ψ equals to q_φ when the flow rule is assumed associated.

It is admitted that the strength properties are significantly degraded in mobilized soil mass during the sliding. In this work, the strain-softening behavior induced by increasing deviatoric plastic strain is used in the D-P model (Fig. 3b), and the corresponding softening rules are defined as

$$c = c_r + (c_p - c_r)e^{-\eta<\varepsilon_{ep}-\varepsilon_{pp}>} \tag{15}$$

$$\varphi = \varphi_r + (\varphi_p - \varphi_r)e^{-\eta<\varepsilon_{ep}-\varepsilon_{pp}>} \tag{16}$$

where, c_r and c_p are residual cohesion and peak cohesion, φ_r and φ_p are residual friction angle and peak friction angle, η and ε_{ep} are shape factor and deviatoric plastic strain, respectively. Moreover, ε_{pp} shows the threshold strain of softening behavior. Regarding Eqs. (15) and (16), the cohesion and friction angle of the soil remain constant for $\varepsilon_{ep} < \varepsilon_{pp}$ (Macaulay brackets $< >$ are used so that only the positive values are taken into account). Once the plastic deviatoric strain exceeds the threshold strain ($\varepsilon_{ep} > \varepsilon_{pp}$), the strength parameters start to reduce and tend to their residual values.

ASCE International Journal of Geomechanics. Submitted Dec 2020; Published Jan 2022.
https://doi.org/10.1061/(ASCE)GM.1943-5622.0002308

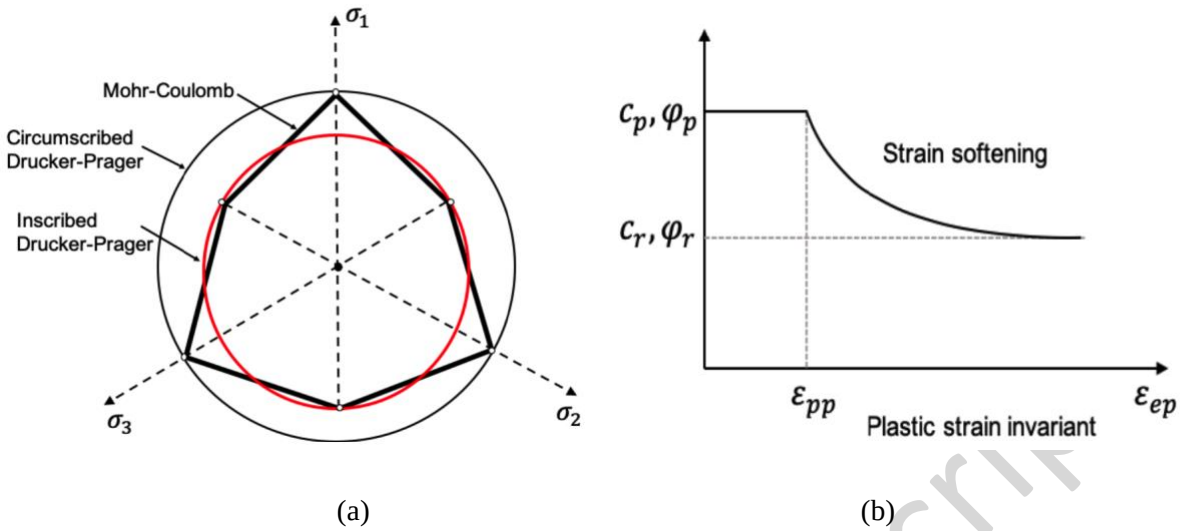

(a) (b)

Fig. 3 (a) Yield surface of the D-P model in π plane; (b) sketch of the strain softening model

Generalized interpolation material point method (GIMP)

MPM is a particle-based mesh-free method which was developed on the basis of the particle-in-cell concept (Sulsky et al. 1994) and has been proven as a promising particle-based method for modeling the behavior of different earth structures under the large strain processes (Soga et al. 2016). MPM consists of two discretizations, including a) a cluster of material points (Lagrangian particles) representing the continuous material which is allowed to move freely and carry the density, strain, stress, and all state variables of the continuous body; and b) a background Eulerian mesh for solving the governing equations and determining incremental velocities, instead of carrying mechanical parameter information. However, the original MPM has cell-crossing instability, which is caused by a discontinuous gradient of shape functions. The generalized interpolation material point method (GIMP) overcomes the instability by allocating each material point its own non-singular domain (Bardenhagen 2002; Bardenhagen and Kober 2004), which has been demonstrated as a stable and useful tool in MPM modeling (Bardenhagen and Kober 2004).

ASCE International Journal of Geomechanics. Submitted Dec 2020; Published Jan 2022.
https://doi.org/10.1061/(ASCE)GM.1943-5622.0002308

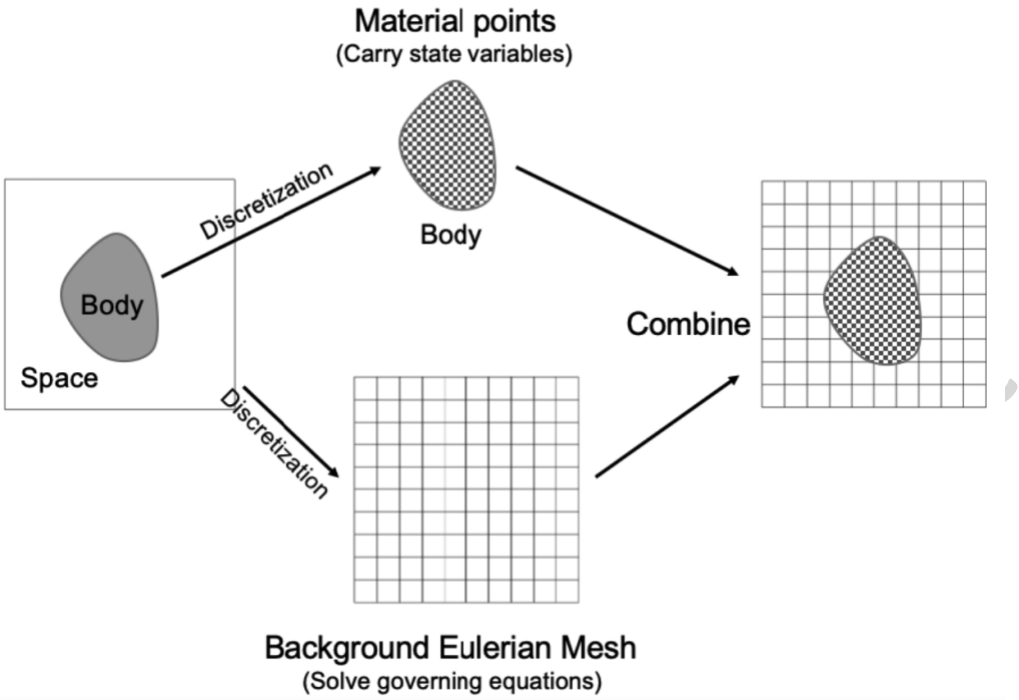

Fig. 4 GIMP discretization

Fig. 4 illustrates the discretization of material body and space using the GIMP which relies on Petrov-Galerkin discretization. A material body within the domain of the problem is discretized into a finite number of material points. In GIMP, the material point is a domain which mass and other variables vary according to a particle characteristic function $\chi_p(x)$ (Bardenhagen and Kober 2004) satisfying the partition of unity property ($\sum_p \chi_p\,(x) = 1, \forall x$). In the particle domain Ω_p, the particle characteristic function has generally been assumed

$$\chi_p(\boldsymbol{x}) = \begin{cases} 1 & \boldsymbol{x} \in \Omega_p \\ 0 & otherwise \end{cases} \tag{17}$$

The function $\chi_p(\boldsymbol{x})$ is used as a basis for representing particle data by giving a material point property f_p (e.g. particle density ρ_p, stress σ_{ijp}, and volume V_p).

ASCE International Journal of Geomechanics. Submitted Dec 2020; Published Jan 2022.
https://doi.org/10.1061/(ASCE)GM.1943-5622.0002308

To discretize the space occupied by the grid, computational grid shape function S_I is introduced and required to be a partition of unity ($\sum_I S_I(x) = 1, \forall x$), which is expressed as

$$S_{Ip} = \frac{1}{V_p} \int_{\Omega_p \cap \Omega} \chi_p(x) N_I d\Omega \tag{18}$$

$$S_{Ip,j} = \frac{1}{V_p} \int_{\Omega_p \cap \Omega} \chi_p(x) N_{I,j} d\Omega \tag{19}$$

where, N_I is the grid nodal shape function, gradients $S_{Ip,j}$ are implicit functions of grid node position x_I, particle position x_p, and current particle volume Ω_p. For this step, the discretization is analogous to FEM. After GIMP discretization, computing the total nodal force f_{iI}

$$f_{iI} = f_{iI}^{int} + f_{iI}^{ext} \tag{20}$$

$$f_{iI}^{int} = -\sum_p \sigma_{ijp} S_{Ip,j} V_p \tag{21}$$

$$f_{iI}^{ext} = \sum_p m_p S_{Ip} b_{ip} + \int_{\Gamma_t} S_I(x) \bar{t}_i d\Gamma_t \tag{22}$$

where, the f_{iI}^{int} is the nodal internal force and f_{iI}^{ext} is the nodal external force at node *I*, respectively. Then, by integrating momentum equations and applying the boundary conditions, the material point position and velocities can be computed. As for the time when the stress is updated, the modified update stress last (MUSL) is adopted in this work, for its better computational stability (Nairn 2003) compared with update stress first (USF) (Bardenhagen 2002) and update stress last (USL) (Sulsky et al. 1994).

ASCE International Journal of Geomechanics. Submitted Dec 2020; Published Jan 2022.
https://doi.org/10.1061/(ASCE)GM.1943-5622.0002308

Random field generation

The failure mode during the landslides is significantly affected by mechanical properties of the soils (e.g., cohesion, internal friction angle, and shear strength) and their inherent spatial variability. Therefore, soil characteristics are defined as RFs, and prior information from their spatial variability are used to calibrate their statistical features which are described by a probability density function with mean value μ and coefficient of variation (COV), and a spatial correlation function (Phoon and Kulhawy 1996; Phoon 2008; Jiang et al. 2014; Liu et al. 2017). Then, using the predefined statistical features, random samples are generated for the soil characteristics to model its spatial variability over the simulation domain. The autocorrelation function (ACF) allows to mathematically characterize the spatial correlation structure between any two points despite their absolute coordinates. It is assumed that the soil characteristics are stationary RFs and their ACF can be defined as a correlation between their quantities at two locations in each sub-domain $H(x, y)$, which is defined mathematically as

$$\rho[H(x_i, y_i), H(x_j, y_j)] = \frac{COV(H(x_i,y_i),H(x_j,y_j))}{\sqrt{Var[H(x_i,y_i)]}\sqrt{Var[H(x_j,y_j)]}} \tag{23}$$

where, $H_i = (x_i, y_i)$ and $H_j = (x_j, x_j)$ are the i and j coordinates of the RFs, COV $(\bullet)$ is the covariance function and Var $(\bullet)$ denotes the variance function. According to relevant literature, DeGroot and Baecher (1993) adopted the Maximum Likelihood Method to estimate the corresponding ACF of the soil shear strength, while Phoon and Ching (2008) estimated the ACF parameters using the method of moments. In general, it is extremely difficult to acquire enough reliable data for specifying and calibrating experimental ACFs of the soil properties due to challenges related to site investigation which is needed to obtain large quantities of geostatistical data. Hence, due to sparse geostatistical data, theoretical ACFs are commonly applied as

alternative functions to characterize the spatial variability of the soil properties (Li and Lumb 1987; Li et al. 2016). Based on the previous research carried out within the concept of the RF theory, the most commonly used theoretical auto-correlation function for simulating inherent spatial variability in geo-slope structures is single exponential (SNX) function (Griffiths and Fenton 2004; Li et al. 2014; Dyson and Tolooiyan 2019). Thus, in this study, the SNX function is used, which can be expressed as

$$\rho(\tau_x, \tau_y) \quad = \exp[-2(\frac{\tau_x}{\delta_h} + \frac{\tau_y}{\delta_v})] \tag{24}$$

where, $\rho(\tau)$ is the correlation coefficients, the $\tau_x = | x_i - x_j |$ and $\tau_y = | y_i - y_j |$ are the absolute distances between two spatial locations in horizontal and vertical directions, respectively; δ_h and δ_v are the scales of fluctuation in horizontal and vertical directions, respectively. The scale of fluctuation δ is used to determine the distance within which the random quantities are highly correlated (Vanmarcke 2010). A small value of δ represents characteristics of a highly heterogeneous soil, while a larger δ signifies the properties of soil with a more homogenous structure. It is significant to estimate an appropriate value of δ, which plays a crucial role in quantifying the spatial variability of the soil properties at field scales. Many researchers (Jaksa et al. 1999; Phoon 2008) studied different approaches of determining the value of scale of fluctuation δ for soil properties and suggested that the scale of fluctuation of the undrained shear strength parameter, S_u, for clayey soil is typically within the horizontal range of 1.0 ~ 92.4 m and the vertical range of 0.1 ~ 8.0 m, respectively. In this work, similar values for S_u are used for simulations.

The Cholesky matrix decomposition (CMD) method (Jiang et al. 2014; Liu et al. 2017) is used to generate RFs in this work, which is easily implementable. Firstly, the domain Ω is discretized into elements of the RF with the centroid coordinates of the elements specified by (x_i, y_i). Therefore, the autocorrelation matrix $\boldsymbol{C}_{n\times n}$, representing the spatial variability of the properties, can be expressed as

$$\boldsymbol{C}_{n\times n} = \begin{bmatrix} 1 & \rho(\tau_{x_{12}}, \tau_{y_{12}}) & \dots & \rho(\tau_{x_{1n}}, \tau_{y_{1n}}) \\ \rho(\tau_{x_{21}}, \tau_{y_{21}}) & 1 & \dots & \rho(\tau_{x_{2n}}, \tau_{y_{2n}}) \\ \vdots & \vdots & \ddots & \vdots \\ \rho(\tau_{x_{n1}}, \tau_{y_{n1}}) & \rho(\tau_{x_{n2}}, \tau_{y_{n2}}) & \dots & 1 \end{bmatrix} \tag{25}$$

where, $\rho(x_{ij}, y_{ij})$ is the auto-correlated coefficient of quantities between the two spatial locations in two dimensions, where τ values represent the absolute distances between the centroid coordinates of the ith particle and the jth particle in horizontal and vertical directions.

Subsequently, the auto-correlation matrix $\boldsymbol{C}_{n\times n}$ can be decomposed into the product of a lower triangular matrix $\boldsymbol{L}$ and a conjugate transpose $\boldsymbol{L}^{\mathbf{T}}$ as follows

$$\mathbf{L} \cdot \mathbf{L}^{\mathbf{T}} = \boldsymbol{C}_{n\times n} \tag{26}$$

where, $\mathbf{L}$ is the lower triangular matrix with a dimension of $n \times n$. Then, a standard Gaussian RF $\boldsymbol{X}^G$ is derived as

$$\boldsymbol{X}^G(x, y) = \mathbf{L} \cdot \xi_i \quad (i = 1,2, \dots, N) \tag{27}$$

where i is the number of standard Gaussian RF, ξ_i is a sample matrix obtained by arranging the vector of n independent standard normal samples as m vectors with dimension of n. Subsequently, the standard Gaussian RF $\boldsymbol{X}^G$ can be used to generate the Non-Gaussian RF $\boldsymbol{X}^{NG}$ of desired values by the isoprobabilistic transformation method. In this paper, the shear strength

parameter (S_u) is considered to be lognormally distributed, the lognormal RF $\boldsymbol{X}^{LN}$ can be generated by

$$\boldsymbol{X}^{LG}(x,y) = exp[\boldsymbol{X}^{G}(x,y)] \quad (i = 1,2,\dots,N) \tag{28}$$

The procedure can be repeated N times to obtain N simulations of the RF.

An RF mesh is generated for a sampling process. The CMD method is employed and a computational algorithm is written to obtain the random samples over the RF mesh. Then, the samples are mapped onto the material points in the MPM (as shown in Fig. 5). The transmission process is based on the spatial relationship between material point and RF mesh element (e.g. a position-to-position mapping process), which is similar to the methodology used in the random FEM (Gironacci et al. 2018; Mousavi Nezhad et al. 2018; Huang et al. 2020). Therefore, the sample values of each element in the RF mesh are assigned to the material points surrounded by that element.

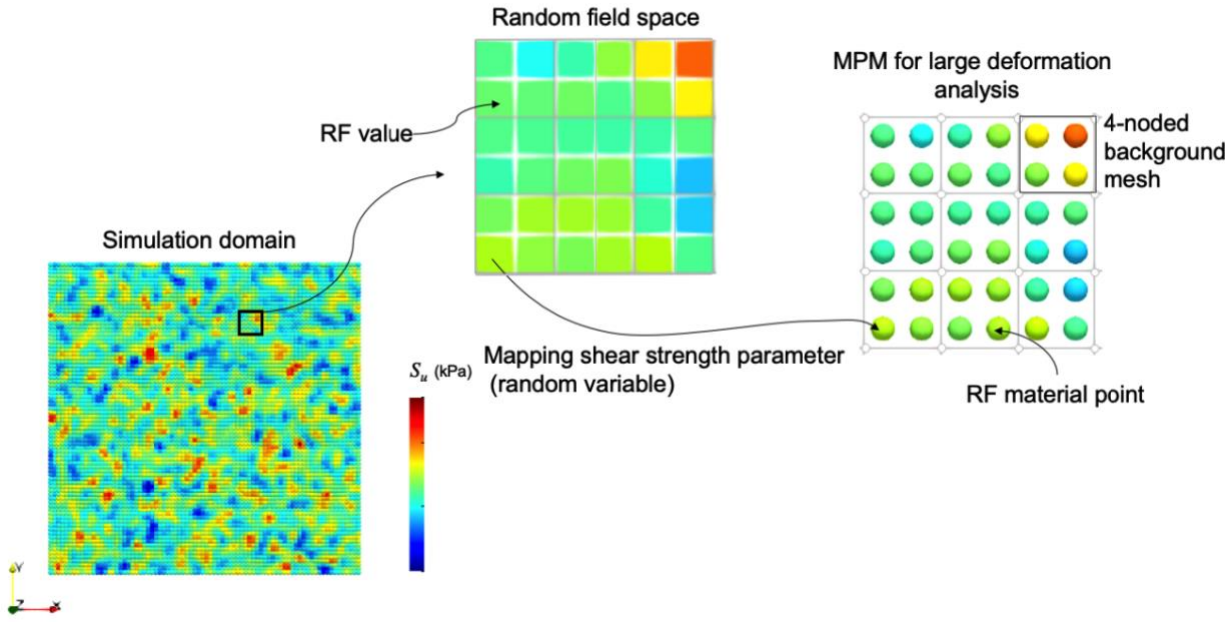

Fig. 5 Schematics of the mapping process of a RF

ASCE International Journal of Geomechanics. Submitted Dec 2020; Published Jan 2022.
https://doi.org/10.1061/(ASCE)GM.1943-5622.0002308

Workflow of the method

The main workflow of simulations with the proposed computational framework in this study can be summarized in the following steps

1. Statistical parameters of the RF and MPM models are introduced to the computational framework.
2. One isotropic Gaussian RF $\boldsymbol{X}^{G}(x, y)$ is generated and subsequently, it is transformed into the lognormal RF $\boldsymbol{X}^{LN}(x, y)$ in the physical space using Eq. (28).
3. The generated sample values are mapped onto the material points and the first simulation of the landslide process is performed to determine influence distance and runout distance.
4. Then, the next RF is generated and updated for the next iteration. It should be noted that after each simulation, the statistical features of the MPM model output (I and R) are calculated. Stages 2 and 3 of the simulations are repeated until convergence of the first and second moments of the model outputs occurs. It is assumed that the convergence occurs when the differences in the calculated values for mean and variance obtained in consequent MC iterations become less than 10^{-3}.
5. All calculated data (I and R) are processed to compute mean values and variances, which are compared with the corresponding deterministic analysis to investigate the effect of spatial variability.

The used MPM code is modified from the openly available MPM3D code (Zhang et al. 2016) (http:\\github.com\xzhang66\MPM3D-F90). The application of the code for landslide analysis has been previously exercised by other researchers (e.g., Li et al. 2016; Liu et al. 2019). In this paper, the MPM3D code is further extended to simulate large deformation behavior in landslide phenomena by allowing the mapping of different generated RFs for soil shear strength onto the

material points. Subsequently, the model can produce estimates of the landslide influence distance, I, and runout distance, R, for each soil variability condition, and associated hazard zone can also be evaluated for the nearby structures that could potentially be influenced by the disaster.

Application to boundary value example

Geometry of the model slope

In this section, a simple clayey slope is modeled to verify the developed framework in simulating the landslide failure mechanism. The slope is considered to have a 5 m height with a length of 25 m and a slope gradient of 45° relative to the horizontal direction. The clay material is also assumed to have a strain-softening behavior. Fig. 6 shows the geometries of the model slope with the corresponding background meshes and material points. The background mesh is extended to 100 m to offer enough space for possible extensive runout distances of the landslide. A frictional contact under the slope base is assumed with a frictional coefficient of 0.3 taken from Bandara and Soga (2015) who presented the characteristics of a similar type of soil. A roller boundary condition is set at the left boundary of the domain to allow vertical material points' movements. Similar model slope was previously analyzed with the deterministic MPM (Bandara and Soga 2015; Wang 2017) as well as the SPH method (Nonoyama et al. 2015; Zhang et al. 2020; Huang et al. 2020); however, the focus of this study is to investigate the effects of spatial heterogeneity in ground's mechanical properties on the large deformations.

ASCE International Journal of Geomechanics. Submitted Dec 2020; Published Jan 2022.
https://doi.org/10.1061/(ASCE)GM.1943-5622.0002308

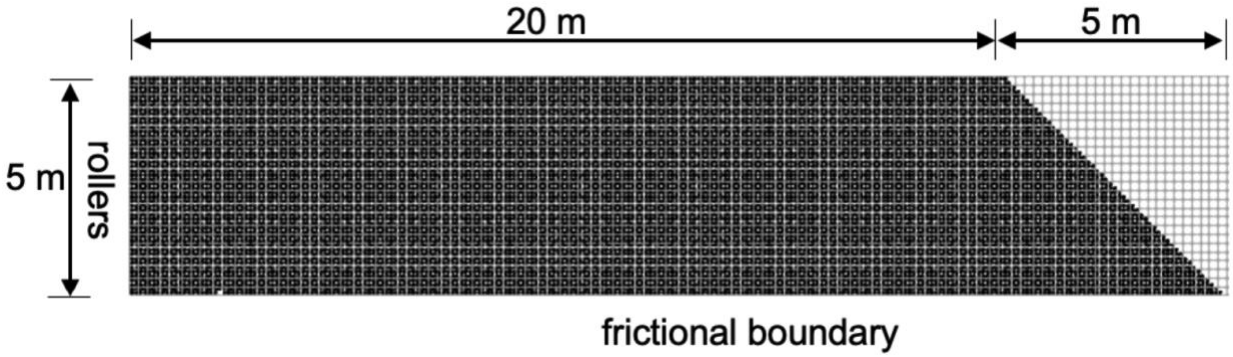

Fig. 6 The initial geometry, boundary conditions, and background mesh of the clay slope

RF and MPM model parameters

Recent studies conducted by Mori et al. (2020) showed that the post-failure behavior of landslides is predominately controlled by the soil's shear strength. The undrained shear strength S_u of the clay is assumed as the spatially random variable; while, Young's modulus E, Poisson's ratio ν, and other soil properties are assumed to be constants as it has been found that their contributions on landslide influence distance or runout distance are not significant (Cheuk et al. 2013). Table 1 shows the statistical parameters of S_u including its mean value μ and COV. Furthermore S_u is assumed to have a logarithmic normal distribution to avoid negative quantities in its sample values. The S_u is interpreted as the peak undrained shear strength S_{up}. The range of fluctuation in the horizontal direction δ_h (varying from 1.0 ~ 92.4 m in the literature for similar soils, e.g. Phoon 2008; Zhang et al. 2018) is selected from 1.0 m (the isotropic soil profile) to 48.0 m (the layered soil profile) because it is closely associated with the uncertainty of slope failure behavior, and the scale of fluctuation in the vertical direction δ_v (usually around 0.1 m to 3 m) is set as 1.0 m (Vanmarcke 2010; Zhang et al. 2018). The properties' values for the representative clay material are summarized in Table 2, which are consistent with previous literature (e.g Wang 2017; Yuan et al. 2020). The constitutive model parameter ε_{pp} is also given a value of 0.1 (Shi et al. 2019). It

should be mentioned that the soil deposit in the presented study is an idealized deposit assuming a soil type that the residual strength of 4 kPa is universally applicable to all elements within the deposit. Therefore, in an unlikely condition if the randomized Sup gets below 4 kPa, it is replaced by the adopted residual value.

Table 1. Statistical parameters of the undrained shear strength S_u

Parameters	unit	Values	Distribution
Mean, μ	kPa	20	Lognormal
COV		0.25	
Horizontal fluctuation, δ_h	m	1, 6, 12, 24, 48	
Vertical fluctuation, δ_v	m	1	

Table 2. Material properties for the clay slope analysis

Parameters	unit	Values
Solid grain density, ρ	kN/m^3	20
Young's modulus, E	kPa	1000
Poisson's ratio, ν		0.33
Peak undrained shear strength, S_{up}	kPa	20
Residual undrained shear strength, S_{ur}	kPa	4

As for the model settings, each realization of S_{up} is generated according to the spatial coordinates (x_i, y_i) at mid-points of the material points in the background mesh in the two dimensions, and then they are mapped onto the material points for calculations. The MPM model contains 11224 material points and 26052 cells, with lengths of 0.1 m for each material point and 0.2 × 0.2 m for

all four-node quadrilateral background cells, resulting in 4 material points in each cell. The minimum values of the scale of the fluctuation (δ_h or δ_v = 1 m) are much larger than 2 times of the cell size (0.2 × 0.2 m), which is consistent with recommendations of Li and Der Kiureghian (1993) to prevent loss of information about the spatial variability of the random field. The landslide is triggered by applying gravitational loading. The time increment is 7.5×10^{-4} s. The total time for the calculation is 15 s when soil deposits become stable according to kinematic energy and unbalanced forces of the system (Kafaji 2013).

Deterministic analysis

Fig. 7 shows the final configuration of a homogeneous landslide computed by deterministic MPM modeling. According to the results, several blocks are formed during the failure process and at t =15.0 s the landslide is completely deposited with an extensive runout motion and substantial retrogressive failure at a new-formed backscarp. For a quantification of the failure consequence, the runout distance with 9.32 m length and influence distance with 18.82 m length can be observed in this figure, which elaborates how long the sliding mass moves and how far the failure retrogresses backwards from the crest of the initial slope to its new-formed backscarp. The results give failure shapes similar to those predicted in previous works, where the influence distance is close to the finding in Wang (2017) (i.e., 9.2 m), and the corresponding runout distance is close to the results of Yuan et al. (2020) (i.e., 18.57 m).

ASCE International Journal of Geomechanics. Submitted Dec 2020; Published Jan 2022.
https://doi.org/10.1061/(ASCE)GM.1943-5622.0002308

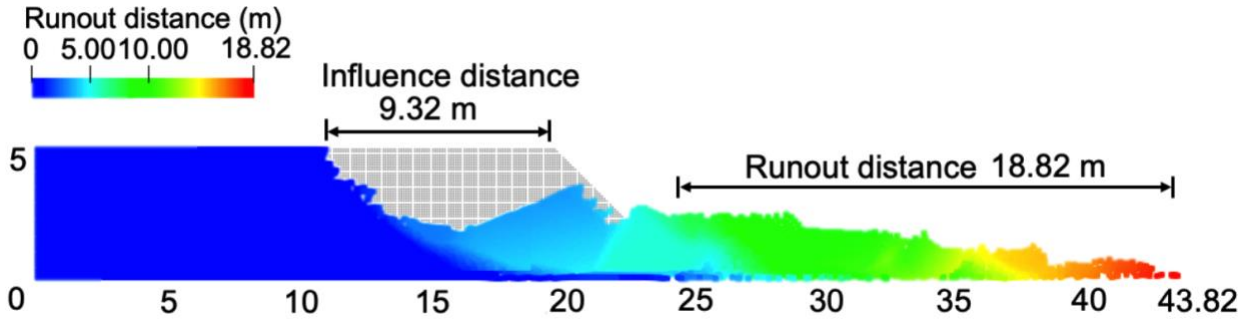

Fig. 7 Initial and final configuration of landslide by deterministic analysis

Typical post-failure process of heterogenous landslides

The influence of spatial variability of undrained shear strength S_{up} on the landslide has been assessed by assuming a COV of 0.25 for peak undrained shear strength S_{up} and different scales of fluctuation (with all other parameters kept identical with the deterministic analysis). In this section, three typical samples of the S_{up} variations over the slope domain are shown in Fig. 8, where the statistically isotropic soil profile RF1 ($\delta_h = \delta_v = 1$m), an anisotropic soil profile RF2 ($\delta_h = 6\ m, \delta_v = 1$ m), and a layered deposited soil profile RF3 ($\delta_h = 48\ m, \delta_v = 1$ m) can be seen. In these figures, the red regions denote the larger S_{up} values, indicating stronger zones, while the blue parts represent the relatively smaller S_{up} values for weaker zones of the slope. In this study, the soil properties are chosen to represent a slope with a very high probability of failure (close to 1.0), in order to investigate the post-failure motions. It should be noted that a particular distribution of a geotechnical RF may lead to predictions demonstrating that the slope is stable, and thus, no post-failure behavior is observed (Liu and Wang 2021). However, consideration of these cases is out of the scope of this study. Given that the main focus here is on analyzing post-failure responses, only cases with a material point displacement larger than 1 m are considered as landslide cases and investigated.

ASCE International Journal of Geomechanics. Submitted Dec 2020; Published Jan 2022.
https://doi.org/10.1061/(ASCE)GM.1943-5622.0002308

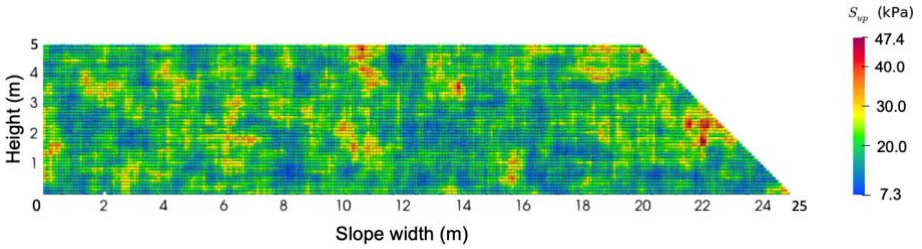

(a) $\delta_h = \delta_v = 1$ m;

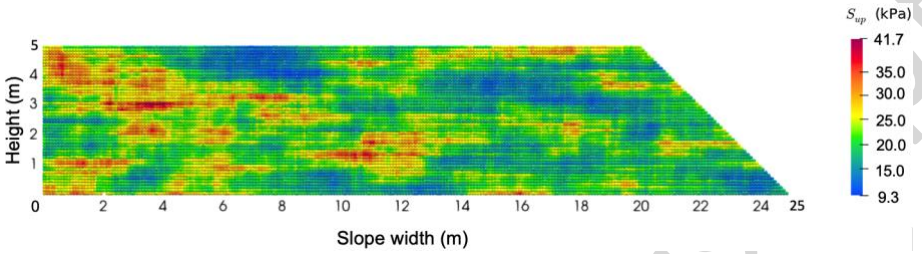

(b) $\delta_h = 6\ m, \delta_v = 1$ m;

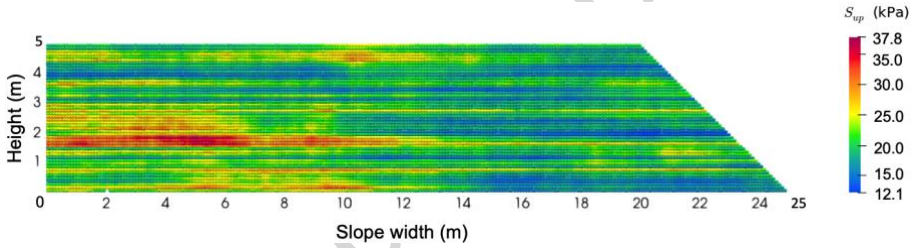

(c) $\delta_h = 48\ m, \delta_v = 1$ m;

Fig. 8 Realizations of S_{up} for three example fluctuation scales

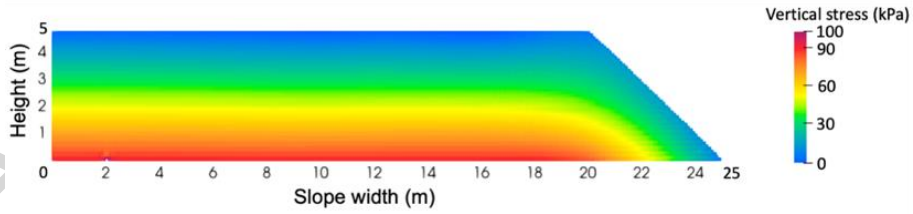

Fig. 9 The initial vertical stress field of the boundary value problem

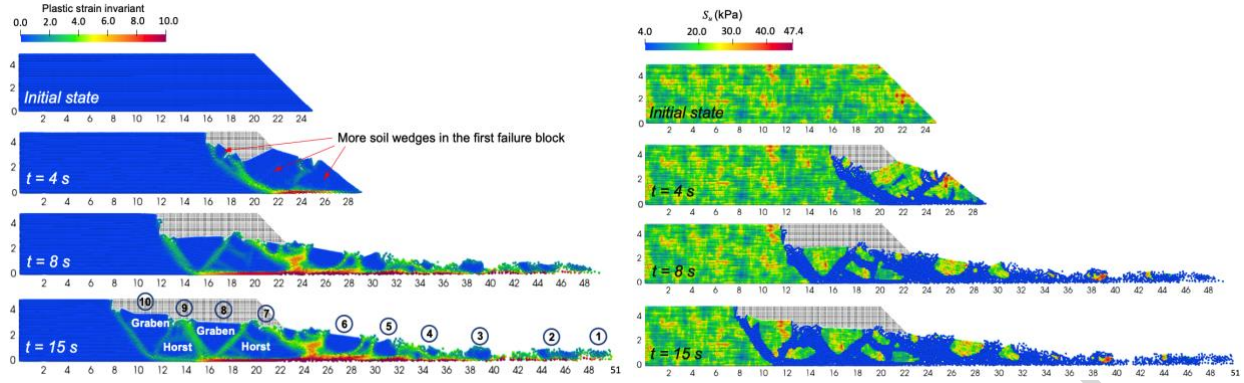

(a) RF1 ($\delta_h = \delta_v = 1$ m);

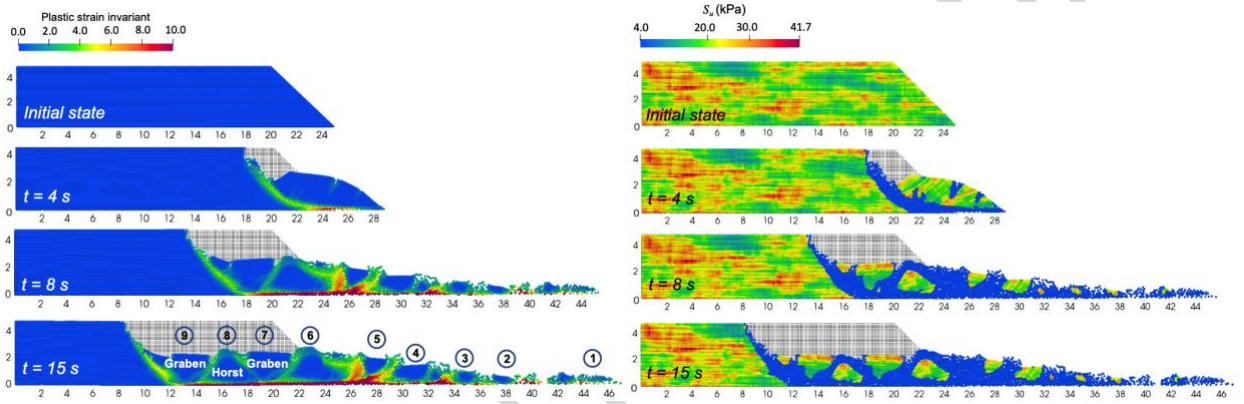

(b) RF2 ($\delta_h = 6\ m, \delta_v = 1$ m);

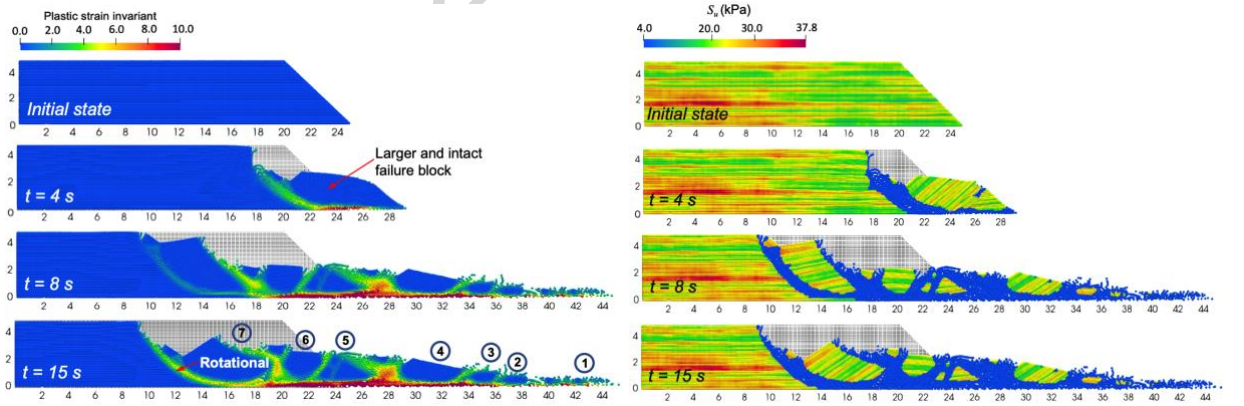

(c) RF3 ($\delta_h = 48\ m, \delta_v = 1$ m);

Fig. 10 The variations of the plastic strain invariant and the distributions of the undrained shear strength, for models with different RFs, at different stages of the analysis leading to failure

ASCE International Journal of Geomechanics. Submitted Dec 2020; Published Jan 2022.
https://doi.org/10.1061/(ASCE)GM.1943-5622.0002308

At the start of the analysis, firstly, by applying a self-weight of the soil mass, *in-situ* stresses are generated within the first 2 s of the simulation (see Fig. 9). As the soil self-weight is applied, the internal stresses start to build up near the slope's toe which is often where failure initiates if the slope becomes unstable. However, because of the distribution of hard soil and soft soil within the slope, the failure initiates above the toe where the safety factor of slope stability N_s is lower, N_s (Steward et al. 2011) is defined as

$$N_s = \frac{S_u}{\rho \cdot H} \tag{29}$$

where H is the actual height of the slope, and ρ is soil density. Therefore, the failure mechanism avoids the stronger zones for seeking out the shear path, which is along the least resistance route and fails along the base of the weaker zones.

Fig 10 shows the typical post-failure movements influenced by δ_h, horizontal heterogeneity, with a colored map of the plastic strain invariant and undrained shear strength, S_u. Various sliding block shapes, a failure processes, and shear bands with different shapes in the final landslide deposits are predicted for different levels of material heterogeneity.

According to the simulated results, three main stages in the heterogeneous landslide failure evolution are concluded: i) the first failure block, ii) the failure of the backscarp, and iii) the final configuration. The first failure block is formed at 4 s. At this stage, the destructuration of the first failure block is more pronounced in RF1 case (Fig.10a), in which more soil wedges can be observed in the first block comparing to that of the RF2 and RF3 case (Fig. 10b and 10c). Due to the large degree of horizontal homogeneity ($\delta_h = 48\ m$), the first failure block in RF3 is relatively bigger and more coherent than in the RF1 and RF2 cases. It is demonstrated that the layered deposited slope is prone to fail in larger/more intact sliding blocks at the initial failure stage

because of the existence of a relatively intact weak intercalation layer (Ma et al. 2018), while the isotropically deposited slope tends to involve more fragmented failure blocks. Subsequently, because of the removal of the support from the soil mass at the backscarp of the first failure block, the failure of the backscarp is triggered and successive failure blocks are formed. Damaged blocks are progressively developed in weak zones until a full failure of the landslide takes place. The 'V-shaped' developed plastic shear bands are distinctively notable in RF1 and RF2, in which several ridges are created by horsts which are separated by grabens. According to the 2014-updated Varnes classification of landslides (Hungr et al. 2014), this type of spreads could be described as an upward progressive failure, which causes a horizontal failure surface propagation upward. The grabens and horsts are the consequence of dislocation, translation, and subsidence of the soil mass above the failure surface. This is a common feature in this type of landslide, such as the Sainte-Monique sensitive clay landslide in 1994 (Locat et al. 2015). The phenomenon can be explained by higher horizontal heterogeneity in RF1 and RF2 compared with RF3, which leads to smaller failure blocks in the sliding mass (divided by the shear bands) following the failure process. Unlike the 'V-shaped' shear band in RF1 and RF2 cases, in the RF3 case, shear bands take mostly a circular shape as the rotational failure continues to propagate. At the last stage, the basal line of the global failure (which mainly horizontally propagates) can be observed in the largest plastic shear strain contours. Other observations include, i) the shapes of the shear bands and formation of the failure blocks are diverse (as discussed above); ii) the numbers of apparent failure blocks in different cases are different. The landslide associated with RF1 tends to form higher number of sliding blocks (i.e. 10 blocks, as in Fig. 10(a)), while in comparison the landslide associated with RF3 appears to have resulted in a lower number of the failure blocks (i.e. 7 blocks, as in Fig.

10(c)). Also, it can be seen that the failure blocks in RF1 are more disintegrated, whereas the corresponding blocks in RF3 are less fragmented.

According to the above analysis, the influence of heterogeneity on the post-failure behavior of landslides is significant. One main conclusion is that the heterogeneous landslide seeks for failing through the weakest zones which can be observed by the shear bands forming across these areas for discrete failure blocks. Because the strata's structure is different in these slopes, the shear band formations, where ruptures occur, are varied. With the increase of the horizontal scale of fluctuation, δ_h, the landslides tend to involve larger and fewer intact failure blocks. For the smaller degree of horizontal homogeneity (i.e., RF1 and RF2), there is a tendency for forming multiple failure blocks because it is easier to seek out a failure path through the weaker soils and avoid the strong soils. For a larger degree of horizontal homogeneity (i.e., RF3), the failure path tries to propagate through the weak zones, and bigger blocks are formed. Note that the results of each realization of RF may differ due to the distribution of shear strength. Consequently, multiple MC simulations are required to reflect the possible post-failure behaviors of heterogeneous landslides.

Statistical analysis of the influence zone

This section is to investigate the influences of spatial variability (i.e., horizontal heterogeneity, COV) on the studied landslide influence zone. The undrained shear strength S_u of the clay is modeled by RFs based on the statistical moments presented in Table 1. For analyzing the uncertainties of influence distance and runout distance of landslides, iterative calculations based on MC simulation are conducted. Firstly, the isotropic case with $\delta_h = \delta_v = 1$ m and COV=0.25 is used to check the convergence of the MC simulation. Fig. 11 shows the statistical mean values and standard deviations of influence distances I and runout distances R of the landslides, plotted as functions of the number of the MC simulations. 1000 samples of spatially varying S_u profiles

are generated and analyzed. Based on the convergence criterion, it is shown that the convergence is achieved after around 600 simulations with a variance of 2.24 and 1.75 for *I* and *R*, respectively. The convergence criteria have been checked for small and large scales of fluctuations. The results for the cases with large scale of fluctuation converge slower (i.e., as the scale of fluctuation increases, the number of MC samples for converging the stochastic model output increases). Eventually, it is observed that the 1000 MC simulations can produce reasonably stable/reliable results in all cases.

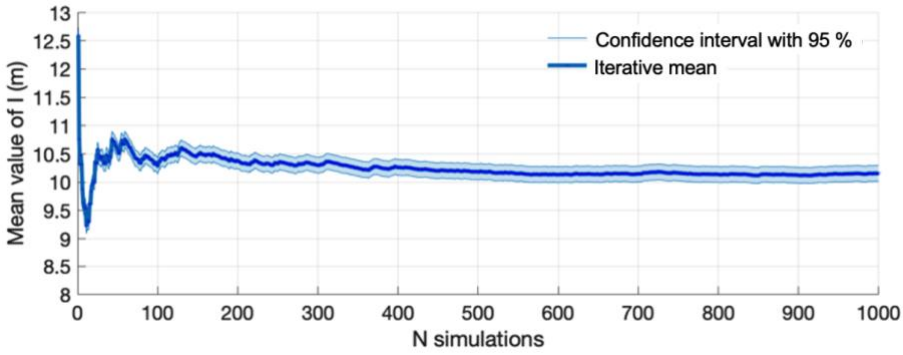

(a)

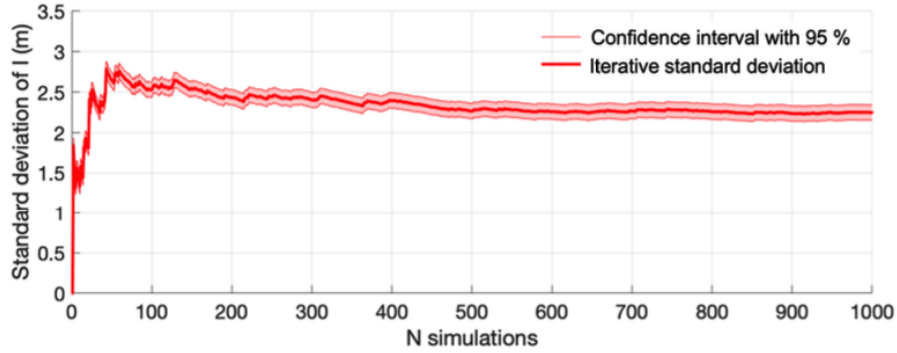

(b)

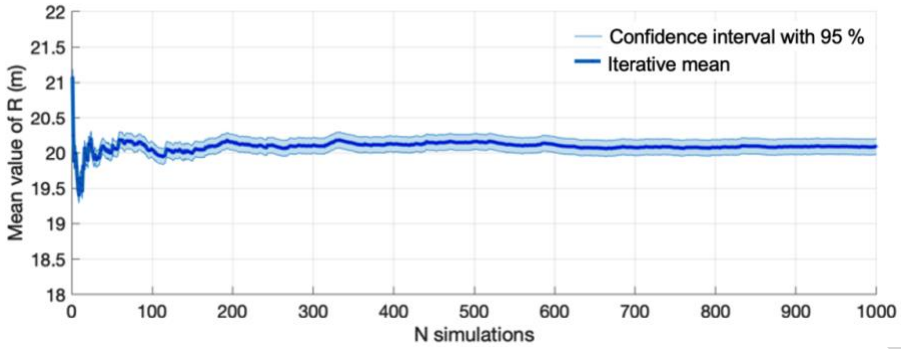

(c)

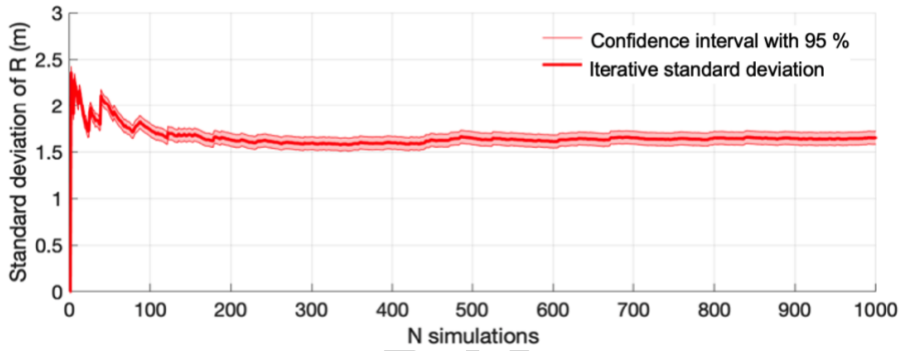

(d)

Fig. 11 Monitoring the convergence of MC simulations: (a) variation of calculated mean value of I with number of simulations; (b) variation of normalized standard deviation of I with number of simulations; (c) variation of calculated mean value of R with number of simulations; (d) variation of normalized standard deviation of R with number of simulations

Effect of the horizontal heterogeneity

Statistical analyses of the influence zone of heterogeneous landslides considering different level of horizontal heterogeneity are performed using results from the MC simulations, where each simulation comprises 1000 samples. Fig. 12a plots the probability density histograms for I from the analyses of the isotropic RF case ($\delta_h = \delta_v = 1\ m$). In the figure, the horizontal coordinate represents the calculated influence distance or calculated runout distance, the left vertical

coordinate represents the probability density functions, and the right coordinate represents the cumulative probability function. The probability density function is obtained by fitting both Normal and Lognormal distribution functions based on the computed values. It can be seen that both distributions could reasonably fit the histogram. According to the Chi-square goodness of fit test, it is confirmed that the Normal distribution could be adopted to characterize the influence distance for all the involved cases at a 5% level of significance. As such, the Normal distribution function will be used to approximate the probability density function of the computed distance. Fig. 12a shows that the estimated mean value of I for δ_h = 1.0 m is 10.15 m. In comparison, the deterministic analysis underestimates the influence distance with 9.32 m, giving an unconservative estimation of the potential retrogressive failure. This is a large discrepancy in post-failure motions between the homogeneous landslide and the heterogenous landslide. Because of the soil heterogeneity, the values for the influence distance mostly varies from 6 m to 14 m, and the maximum influence distance can reach up to 17.3 m. This demonstrates the high degree of uncertainty in prediction of the influence distance, that necessitates incorporating the effect of natural heterogeneity of soil in modeling of post-failure process.

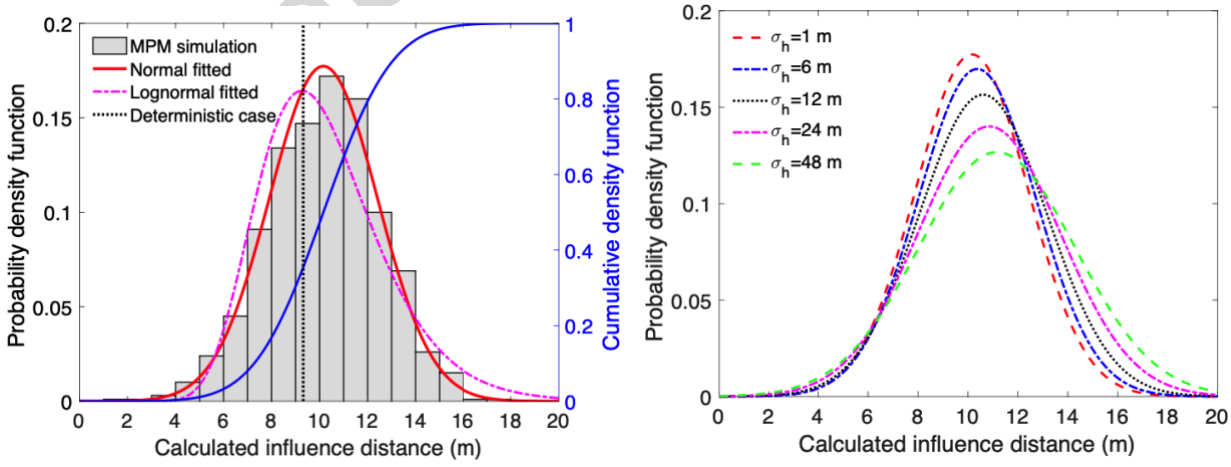

(a) $\delta_h = \delta_v = 1$ m (b) Effect of δ_h on the probability density function

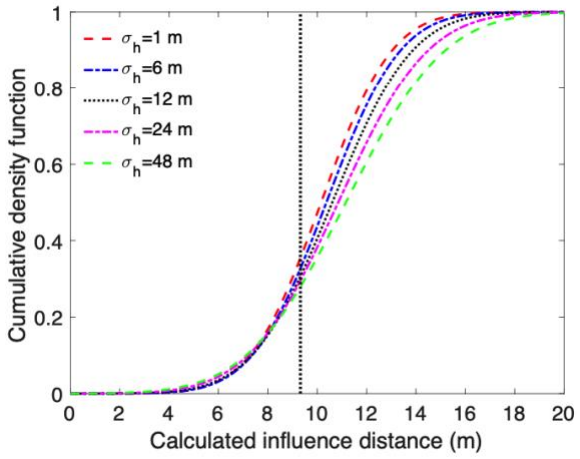

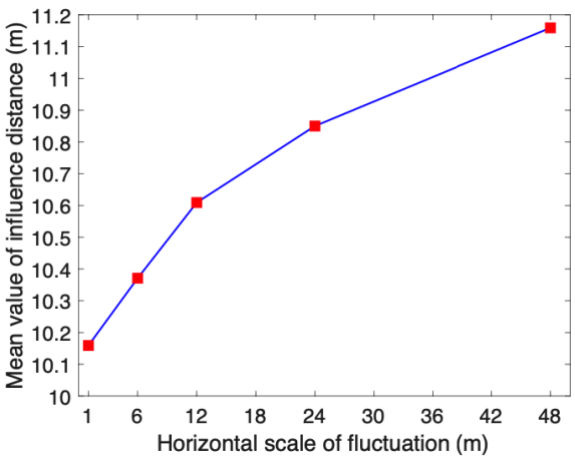

(c) Effect of δ_h on the cumulative density function (d) Influence of δ_h on mean value

Fig. 12 Histogram, probability density functions, cumulative density functions, and mean values of the influence distance I

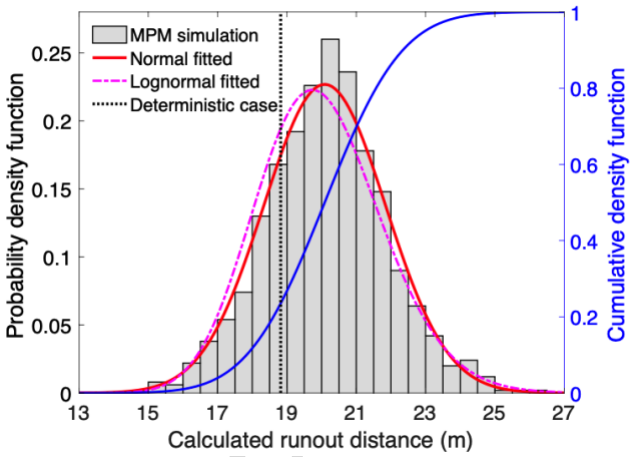

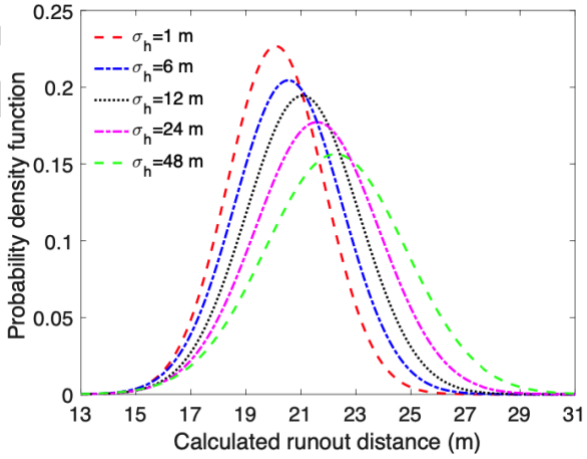

(a) $\delta_h = \delta_v = 1$ m (b) Effect of δ_h on the probability density function

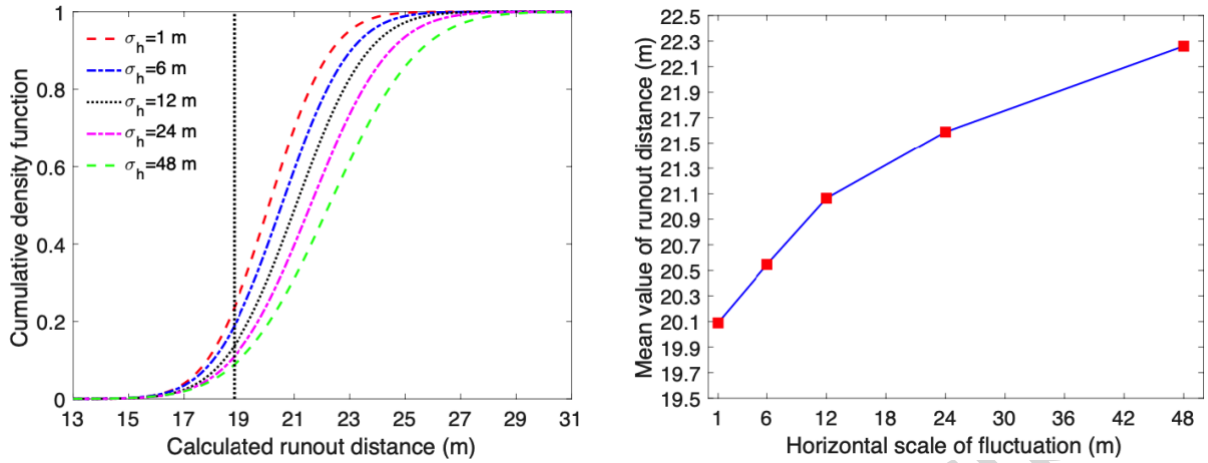

(c) Effect of δ_h on the cumulative density function (d) Influence of δ_h on mean value

Fig. 13 Histogram, probability density functions, cumulative density functions, and mean values of the runout distance *R*

To comprehensively study the effect of δ_h on the influence distance, the corresponding normal-fitted probability density function curves are plotted and compared in the Fig. 12b. Among the different δ_h, it can be found that horizontal heterogeneity of shear strength in the slope not only causes variations in the mean values of *I* but also affects the shape of the corresponding probability density function. The probability density function curves become wider, lower, and farther to the right with the increase of δ_h, which indicates that the increasing of δ_h would increase the probabilities of occurrence of extreme case of the studied landslide in terms of influence distance. For instance, the probability of I =18 m in the $\delta_h = 48$ m case is much higher than the other cases. According to the statistics (Fig. 12d), it shows that the mean values of *I* slightly increase with increasing δ_h, which indicates as the horizontal heterogeneity decreases the landslides tend to form a longer influence distance. The residual part of the topside tends to be smaller with smaller horizontal heterogeneity. Based on the cumulative density function curves (Fig. 12c), the probability of results exceeding the deterministic prediction is determined. The gaps between the

deterministic analysis and the mean value of the RF cases are considerable, where about 68% of all samples exceed the deterministic case ($I \geq 9.32$ m); in particular, results of about 72% of samples with $\delta_h = 48$ m exceed the deterministic analysis.

As shown in Fig. 13a, the probability density histogram represents the calculated *R* of the isotropic RF case from 1000 MC simulations. Similar with the computed *I*, the values for the *R* vary significantly, which is mostly in the range of 17 m to 24 m; the minimum runout distance is 15.08 m, and the maximum runout distance can reach up to 27.00 m; the mean value is 20.08 m. In comparison, the deterministic analysis particularly underestimates the runout distance with 18.82 m, which may give an nonconservative/unsafe estimation of the potential risks for the structures located in the vicinity of slopes. As previously described, the Normal distribution function is adopted to approximate the probability density function of the computed distance. Through comparing the Normal-fitted probability density function curves (Fig. 13b), it is seen that δ_h of shear strength in the slope not only causes variations in the mean values of *R* but also affects the shape of the corresponding probability density function. The probability density function curves become wider, lower, and farther to the right with the increase in δ_h. The mean values of *R* tend to increase with increasing δ_h (i.e., decreasing horizontal heterogeneity), and consequently the landslides tend to form relatively longer runout distance (Fig. 13d). The maximum mean value of 22.26 m is obtained from the case of $\delta_h = 48\ m$. This could partly be explained by a common unfavorable geological structure in bedding landslides, in which large intact and strong geomaterials are overlying the relatively weak geomaterial layers (weak intercalated layer). This type of geological structure could easily lead to large-scale long runout landslides (Ma et al 2018). Furthermore, extreme cases (i.e., landslide with exceptionally long runout) could happen with larger δ_h. Based on the cumulative density function curves (Fig. 13c), the probability of exceeding

the deterministic analysis is obtained, which shows about 75% of all samples exceed the deterministic case ($R \geq 18.82$ m). Therefore, the influence of spatial variability of undrained shear strength on the influence zone is not insignificant. The mean values of both computed I and R in landslides tend to increase with increasing δ_h of the ground profile, and the standard deviation (variance) generally enlarges with increasing δ_h as well. It indicates that the uncertainty of the influence zone (I and R) will be reduced when δ_h decreases. In other words, neglecting the horizontal heterogeneity of shear strength will lead to underestimation of the landslide influence zone.

Effect of the COV

For the previous analyses, the COV of undrained shear strength S_u are fixed as shown in Table 1. In order to discuss the effect of the COV on the probabilistic results, different values are used for the COV of S_u. According to the previous studies on uncertainty properties of S_u, the COVs are selected within the bounds of $0.1 \leq \text{COV} \leq 0.5$ (Phoon and Kulhawy, 1996; Phoon, 2008; Zhang et al. 2018).

Fig. 14 presents the Normal-fitted mean values and standard deviations of the influence distance and runout distance in the landslides with different COVs of the S_u and $\delta_h = \delta_v = 1$ m. It can be clearly observed that the COV has a non-negligible effect on the mean value and standard deviation of the I and R. With the increasing of COV, the range of the influence distance as well as runout distance increase, which means the increasing COV will enlarge the uncertainty and randomness of the landslide's influence zone. As shown in Fig. 14, the standard deviation of both I and R increases with the increase of COV. These results are consistent with those from other studies (Zhang et al. 2020). As for a small COV, the mean value of runout distance will be more

conservative, and large values of COV result in a bigger runout distance. Because higher COV values of shear strength would lead to larger range of shear strength in some parts of the slope, the uncertainty of associated post-failure motions would increase as well. Consequently, much larger influence zone is revealed by considering the large degree of variation compared to the relatively small heterogeneity case.

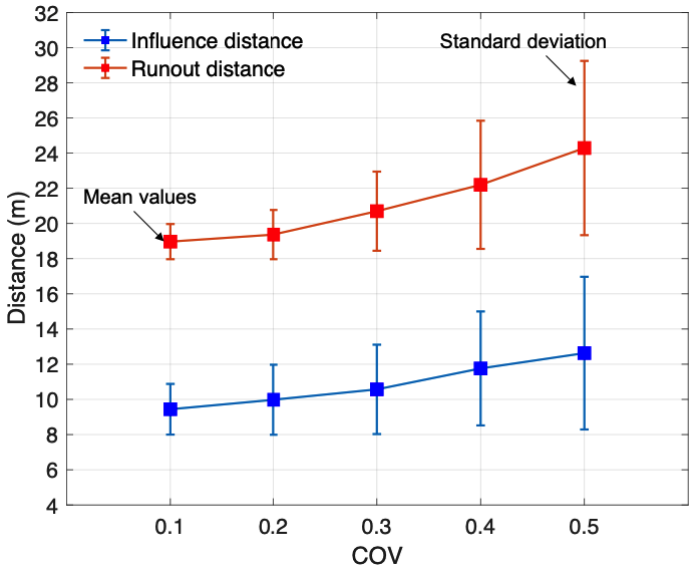

Fig. 14 Effect of the COV (0.1-0.5) on the influence distance and runout distance for isotropic cases ($\delta_h = \delta_v = 1$ m)

Hazard zoning of landslides

Apart from I and R predictions for heterogenous landslides, a practical hazard zoning analysis is carried out for common structures, e.g. buildings, railway, etc., that are located at the slope toe or crest and might be susceptible to landslide post-failure. To rank the potential hazard, the likelihood classification of disaster events proposed by Lacasse and Nadim (2011) is adopted (Table 3). This study considered exceedance probabilities of 0.1%, 1%, 10%, 50% as threshold values. The exceedance probabilities of $P(I > I_s)$ and $P(R > R_s)$ obtained by Eq. (1-4) reflects the possibility

that a certain point along the motion path is at risk. The area potentially influenced by the landslide is classified into five groups, namely: extremely high, high, medium, low and extremely low, according to the range of P.

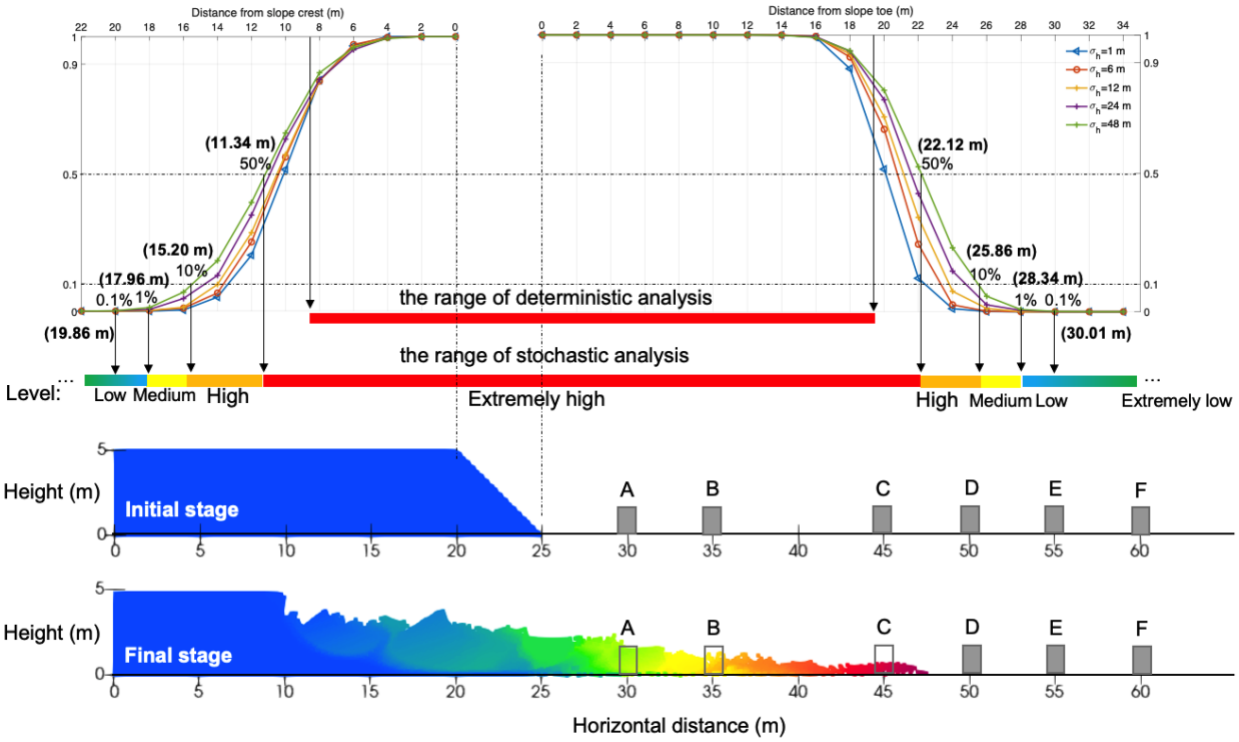

Fig. 15 Hazard zoning of landslides

Fig. 15 shows a set of I and R exceedance probability curves with different δ_h and COV= 0.25, in which the potential hazard zoning of the landslide is highlighted according to the classification. Each curve in the figure approximates the exceedance probability that the failure would affect the structure at different distances away from the slope's toe or crest (R_s and I_s). According to the results, the $P(I > I_s)$ decreases as the distance from the initial crest of the slope increases, and $P(R > R_s)$ decreases as the distance from the initial toe of the slope increases. It can be found that among the different δ_h cases, bigger δ_h tends to form a wider range of influence zone and constitutes higher hazard levels than the other cases, since higher probabilities can be observed at

the same I_s or R_s. If considering the δ_h=48 m as the worst case, when $I_s < 11.34$ m and $R_s < 22.12$ m, these areas belong to extremely high hazardous zones (specified by red shaded area in Fig. 15) according to the classification (see table 3). Then, the hazard zones gradually transform to high level (specified by orange shaded area) at $11.34\,m < I_s < 15.20$ m and $22.12\,m < R_s < 25.86$ m, when the $P(I > I_s)$ and $P(R > R_s)$ decrease from 50% to 10%. When the exceedance probability decreases to approximately 1%, $I_s = 17.96$ m and R_s= 28.34 m are taken as boundaries to separate the low and medium hazard levels, when considering the worst cases.

For illustration, by assuming that there are structures located from point A to point F at different distances away from the initial toe of the slope, a random heterogeneous case has been modeled. It can be easily found that the structures A, B, C would certainly be affected by the landslide motion at the final stage. However, the structure C would not be affected if we only consider the deterministic analysis. The range of the deterministic analysis is comparably limited, while considering the spatial variability the area remains at high hazard level when the I is larger than 9.32 m and R is larger than 18.82 m. For instance, the structures D and E still face the potential impacts from the landslide, because they fall in the medium and low level zones, respectively. As for the extremely low hazard level, the structure F should be constructed at least 30 m away from the toe to be safe. Based on the above hazard zoning analysis, the proposed method can be applied as a practical measure, serving as a disaster indicator for hazard management and mitigation plans.

Table 3. Event likelihood classification (adapted from Lacasse and Nadim (2011))

Verbal description of uncertainty	Description	Event probability
Virtually certain	Event, owing to known physical conditions or processes that can be described and specified with almost complete confidence	0.999
Very likely	Event is highly likely, but may not occur, although one would be surprised if it did not occur	0.990
Likely	Event is likely, but may not occur	0.90
Completely uncertain	There is no reason to believe that one outcome is any more or less likely to occur than the other	0.50
Unlikely	Event is unlikely, but it could occur	0.10
Very unlikely	The possibility cannot be entirely ruled out on the basis of physical or other reasons	0.01
Virtually impossible	Event, owing to known physical conditions or processes, can be ruled out with almost complete confidence	0.001

Conclusions

With the current changes in climate, severe and rapid rainfalls, seismic excitations, etc., many natural slopes are susceptible to landslide risk. Hence understanding post-failure behavior of landslides is significantly important as it paves the way for the prediction of possible catastrophic consequences and timely planning of the disaster mitigation measures. To this end, the main aim of this study was to investigate the post-failure behavior and the probable influence zone in the case of landslides; and, as such the soil properties have been chosen to represent a slope with a very high probability of failure (close to 1.0) to investigate the post-failure motions. The paper

proposes the use of a new stochastic numerical modeling framework, on the basis of the material point method (MPM) and random field (RF) theory, to: i) quantify the uncertainties of RF parameters (δ_h and COV) of shear strength employed in the large deformation geotechnical model; ii) quantitatively evaluate the exceedance probability of influence zone for heterogeneous landslides; iii) plot a practical landslide hazard zoning map in terms of disaster mitigation. The effects of soil inherent heterogeneity in the post-failure modeling of landslides were comprehensively investigated. The main conclusions obtained from the analyses presented in this paper can be summarized as follows:

1. The spatial variability of S_u notably influences the failure mode of the landslide, and consequently its post-failure behavior and influence zone. Different soil profile compositions in the slope result in different failure paths and mechanisms. A slope with larger δ_h would tend to experience larger failure blocks and longer runout/influence distances in a landslide failure scenario.
2. After comparing the results of both homogeneous and heterogeneous models, it is found that with the condition that the S_{ur} = 4 kPa relative to S_{up} = 20 kPa and COV= 0.25, the homogeneous soil profile yields unsafe predictions leading to an underestimation of the landslide influence zone. While a heterogeneous soil profile in a slope under landslide conditions would show significant variations in the influence zone. Furthermore, a much larger influence zone is predicted by considering the large COV of the shear strength compared to the case with relatively small heterogeneity. This demonstrates the necessity to take soil spatial heterogeneity into consideration for post-failure modeling of the landslides.
3. The proposed hazard zoning framework can be considered as a practical tool to facilitate the evaluation of hazard levels concerning the impacts of a landslide on neighboring structures

or facilities by using a set of exceedance probability curves. The approach allows quantitative disaster assessments associated with landslide instability, hence enabling hazard zoning or priority ranking for various mitigation measures considering the uncertainty and/or tolerable risk levels.

Although the framework is used for simulation of a univariate RF of a specific slope, it is a general framework and can be extended to consider various soil properties as well as precipitation, seismic acceleration as multivariate geotechnical RFs. Other slope geometries also can be replaced in this framework if the main consideration is impacts/hits on nearby structures by extensive runout or retrogressive failure.

Data Availability Statement

All data, models, and code generated or used during the study appear in the submitted article.

Reference

Andersen, S., and L. Andersen. 2010. "Modelling of landslides with the material-point method." *Comput. Geosci.* 14: 137–147.

Bandara, S., and K. Soga. 2015. "Coupling of soil deformation and pore fluid flow using material point method." *Comput. Geotech.* 63: 199-214.

Bardenhagen, S. G. 2002. "Energy conservation error in the material point method for solid mechanics." *J. Comput. Phys.* 180 (1): 383-403.

Bardenhagen, S. G., and E. M. Kober. 2004. "The generalized interpolation material point method." *C. Comput. Model. Eng. Sci.* 5: 477-495.

Bishop, A. W., J. N. Hutchinson, A. D. M. Penman, and H. E. Evans. 1969. "Geotechnical investigation into the causes and circumstances of the disaster of 21 October 1966". A selection of technical reports submitted to the Aberfan Tribunal. HMSO, The Stationary Office Ltd., Norwich, UK,

1-80.

Brand, E. W., J. Premchitt, and H. B. Phillipson. 1984. "Relationship between rainfall and landslides in Hong Kong." In Proceedings of the 4th International Symposium on Landslides, 1(01): 276-84.

Cheuk, C. Y., K. K. S. Ho, A. Y. T. Lam. 2013. "Influence of soil nail orientations on stabilizing mechanisms of loose fill slopes." *Can. Geotech. J.* 50(12):1236-1249.

DeGroot, D. J., and G. B. Baecher. 1993. "Estimating autocovariance of in-situ soil properties". *J. Geotech. Eng.* 119(1):147-166.

Dyson, A. P., and A. Tolooiyan. 2019. "Prediction and classification for finite element slope stability analysis by random field comparison." *Comput. Geotech.* 109:117-129.

Gironacci, E., M. Mousavi Nezhad, M. Rezania, G. A. Lancioni. 2018. "Non-local probabilistic method for modeling of crack propagation." *Int. J. Mech. Sci.* 144:897–908.

Griffiths, D. V., and G. A. Fenton. 2004. "Probabilistic Slope Stability Analysis by Finite Elements." *J. Geotech. Geoenvironmental. Eng.* 130:507–518.

He, K., G. Ma, X. Hu, G. Luo, X. Mei, B. Liu, et al. 2019. "Characteristics and mechanisms of coupled road and rainfall-induced landslide in Sichuan China." *Geomatics. Nat. Hazards. Risk.* 10:2313–2329.

Hicks, M. A., and K. Samy. 2002. "Influence of heterogeneity on undrained clay slope stability." *Q. J. Eng. Geol. Hydrogeol.* 35:41–49.

Huang, P., S. Li, H. Guo, Z. Hao. 2015. "Large deformation failure analysis of the soil slope based on the material point method." *Comput. Geosci.* 19:951–963.

Huang, R., and X. Fan. 2013. "The landslide story." *Nat. Geosci.* 6:325–6.

Huang, Y., G. Li, M. Xiong. 2020. "Stochastic assessment of slope failure run-out triggered by earthquake ground motion." *Nat. Hazards.* 101:87–102.

Hungr, O., S. Leroueil, L. Picarelli. 2014. "The Varnes classification of landslide types, an update." *Landslides* 11:167–94.

Iverson, R. M., D. L. George, K. Allstadt, M. E. Reid, B. D. Collins, J. W. Vallance, ... and J. B. Bower 2015. "Landslide mobility and hazards: implications of the 2014 Oso disaster." *Earth and Planetary Science Letters* 412: 197-208.

Jaksa, M. B., W. S. Kaggwa, P. I. Brooker. 1999. "Experimental evaluation of the scale of fluctuation of a stiff clay." *8th Int. Conf. Appl. Stat. Probab. Civ. Eng.* 1:415-422.

Jiang, S. H., D. Q. Li, L. M. Zhang, C. B. Zhou. 2014. "Slope reliability analysis considering spatially variable shear strength parameters using a non-intrusive stochastic finite element method." *Eng. Geol.* 168:120–128.

Jibson, R. W. 2006. "The 2005 La Conchita, California, landslide". *Landslides* 3(1): 73-78.

Kafaji, I. K. J. 2013. "Formulation of a Dynamic Material Point Method (MPM) for Geomechanical Problems" Ph.D thesis. Germany: University of Stuttart.

Lacasse, S., F. Nadim. 1997. "Uncertainties in characterising soil properties." *Publ-NGI.* 201: 49-75.

Lacasse, S., F. Nadim. 2011. "Learning to live with geohazards: from research to practice." *Geo-risk: risk asssessment and management*:64-116.

Li, C., K. A. Der. 1993. "Optimal Discretization of Random Fields." *Eng. Mech.* 119(6):1136-1154.

Li, D. Q., H. X, K. K. Phoon, L. M. Zhang, C. B. Zhou. 2014. "Effect of spatially variable shear strength parameters with linearly increasing mean trend on reliability of infinite slopes." *Struct. Saf.* 49:45–55.

Li, D. Q., T. Xiao, Z. J. Cao, K. K. Phoon. 2016. "Efficient and consistent reliability analysis of soil slope stability using both limit equilibrium analysis and finite element analysis." *Appl. Math. Model.* 40:5216–5229.

Li, K. S., P. Lumb. 1987. "Probabilistic design of slopes." *Can. Geotech. J.* 24(2), 520-535.

Li, X. P., Y. Wu, S. He, L. Su. 2016. "Application of the material point method to simulate the post-failure runout processes of the Wangjiayan landslide." *Eng. Geol.* 212:1–9.

Liu, X. and Y. Wang. 2021. "Probabilistic simulation of entire process of rainfall-induced landslides

using random finite element and material point methods with hydro-mechanical coupling." *Comput. Geotech.* 132, p.103989.

Liu, L. L., Y. M. Cheng, S. H. Jiang, S. H. Zhang, X. M. Wang, Z. H. Wu. 2017. "Effects of spatial autocorrelation structure of permeability on seepage through an embankment on a soil foundation." *Comput. Geotech.* 87:62–75.

Liu, K., Y. Wang, M. Huang, and W. H. Yuan. 2021. "Postfailure Analysis of Slopes by Random Generalized Interpolation Material Point Method." *Int. J. Geomech*. 21(3), p.04021015.

Liu, X., Y. Wang, D. Q. Li. 2019. "Investigation of slope failure mode evolution during large deformation in spatially variable soils by random limit equilibrium and material point methods." *Comput. Geotech.* 111.

Llano-Serna, M. A., M. M. Farias, D. M. Pedroso. 2016. "An assessment of the material point method for modelling large scale run-out processes in landslides." *Landslides* 13:1057–1066.

Locat, A., S. Leroueil, A. Fortin, D. Demers, H. P. Jostad. 2015. "The 1994 landslide at Sainte-Monique, Quebec: Geotechnical investigation and application of progressive failure analysis." *Can. Geotech. J.* 52(4):490-504.

Ma, G., X. Hu, Y. Yin, G. Luo, Y. Pan. 2018. "Failure mechanisms and development of catastrophic rockslides triggered by precipitation and open-pit mining in Emei, Sichuan, China." *Landslides* 15:1401–1414.

Mafi, R., S. Javankhoshdel, B. Cami, R. Jamshidi Chenari, and A. H. Gandomi. 2020. "Surface altering optimisation in slope stability analysis with non-circular failure for random limit equilibrium method." *Georisk: Assessment and Management of Risk for Engineered Systems and Geohazards,* 1-27.

Masoudian, M. S., A. M. A. Hashemi, A. Tasalloti, A. M. Marshall, 2019. "A general framework for coupled hydro-mechanical modelling of rainfall-induced instability in unsaturated slopes with multivariate random fields." *Comput. Geotech.* 115:103162.

Mori, H., X. Chen, Y. F. Leung, D. Shimokawa, M. K. Lo. 2020. "Landslide hazard assessment by smoothed particle hydrodynamics with spatially variable soil properties and statistical rainfall distribution." *Can. Geotech. J.* 57(12):1953-1969.

Mousavi Nezhad. M. 2010. "Stochastic Finite Element Modelling of Flow and Solute Transport in Dual Domain System" Ph.D thesis. United Kingdom: University of Exeter.

Mousavi Nezhad. M., A. A. Javadi, A. Al-Tabbaa, F. Abbasi. 2013. "Numerical study of soil heterogeneity effects on contaminant transport in unsaturated soil (model development and validation)." *Int. J. Numer. Anal. Methods. Geomech.* 37:278–298.

Mousavi Nezhad. M., E. Gironacci, M. Rezania, N. Khalili. 2018. "Stochastic modelling of crack propagation in materials with random properties using isometric mapping for dimensionality reduction of nonlinear data sets." *Int. J. Numer. Methods. Eng.* 113:656–680.

Nairn, J. A. 2003. "Material point method calculations with explicit cracks." *Comput. Model. Eng. Sci.* 6:649-664.

Nonoyama, H., S. Moriguchi, K. Sawada, A. Yashima. 2015. "Slope stability analysis using smoothed particle hydrodynamics (SPH) method." *Soils. Found.* 55:458–570.

Phoon, K. K., F. H. Kulhawy. 1996. "On quantifying inherent soil variability." *Geotech. Spec. Publ.* 58:326-340.

Phoon, K. K. 2008. "Reliability-based design in geotechnical engineering: Computations and applications." CRC.

Reddy, J. N. 2013. "An Introduction to Continuum Mechanics," Cambridge university press. Second ed.

Rezania, M., N. Sivasithamparam, and M. Mousavi Nezhad. 2014. "On the stress update algorithm of an advanced critical state elasto-plastic model and the effect of yield function equation." Finite Elements in Analysis and Design, 90, 74-83.

Rezania, M., H. Nguyen, H. Zanganeh, and M. Taiebat. 2018. "Numerical analysis of Ballina test

embankment on a soft structured clay foundation." Computers and Geotechnics, 93, 61-74.

Shi, B., Y, Zhang., and W. Zhang. 2019. "Run-out of the 2015 Shenzhen landslide using the material point method with the softening model." Bulletin of Engineering Geology and the Environment, 78(2), 1225-1236

Soga, K., E. Alonso, A. Yerro, K. Kumar, S. Bandara. 2016. "Trends in large-deformation analysis of landslide mass movements with particular emphasis on the material point method." *Geotechnique* 66(3):248–273.

Steward, T., N. Sivakugan, S. K. Shukla, B. M. Das. 2011. "Taylor's Slope Stability Charts Revisited." *Int. J. Geomech.* 11(4):348-352.

Sulsky, D., Z. Chen, H. L. Schreyer. 1994. "A particle method for history-dependent materials." *Comput. Methods. Appl. Mech. Eng.* 118:179–196.

Vanmarcke, E. H. 1997. "Probabilistic Modeling of Soil Profiles." *J. Geotech. Eng. Div.* 103:1227–46.

Vanmarcke, E. H. 2010. "Random Fields: Analysis and Synthesis." World scientific.

Wang, B., P. J. Vardon, M. A. Hicks, Z. Chen. 2016. "Development of an implicit material point method for geotechnical applications." *Comput. Geotech.* 71:159–167.

Wang, B. 2017. "Slope failure analysis using the material point method" Ph.D thesis. Nertheland: Delft university of technology.

Yerro, A. 2015. "MPM modelling of landslides in brittle and unsaturated soils" Ph.D thesis. Spain: Universitat Politècnica de Catalunya.

Yin, Y., F. Wang, P. Sun. 2009. "Landslide hazards triggered by the 2008 Wenchuan earthquake, Sichuan, China." *Landslides* 6:139–52.

Yin, Y., B. Li, W. Wang, L. Zhan, et al. 2016. "Mechanism of the December 2015 Catastrophic Landslide at the Shenzhen Landfill and Controlling Geotechnical Risks of Urbanization." *Engineering* 2:230–49.

Yuan, W. H., K. Liu, W. Zhang, B. Dai, Y. Wang. 2020. "Dynamic modeling of large deformation

slope failure using smoothed particle finite element method." *Landslides* 17:1591–603.

Zhang, X., Z. Chen, Y. Liu. 2016. "The Material Point Method: a continuum-based particle method for extreme loading cases." Academic Press.

Zhang, L., J. Li, X. Li, J. Zhang, H. Zhu. 2018. "Rainfall-induced soil slope failure: Stability analysis and probabilistic assessment." CRC Press.

Zhang, W, J. Ji, Y. Gao, X. Li, C. Zhang. 2020. "Spatial variability effect of internal friction angle on the post-failure behavior of landslides using a random and non-Newtonian fluid based SPH method." *Geosci. Front.* 11(4):1107-1121.

Zhu, H., and L. M. Zhang. 2013. "Characterizing geotechnical anisotropic spatial variations using random field theory." *Can. Geotech. J.* 50:723–34.